

Toward General Quantum Control with Physics-Informed Large Language Models

Yusheng Zhao^{1†}, Han Wang^{1†}, Xin Liu^{2†}, Xinjie Song³, Jixi He⁴,
Lingwei Song⁵, Yuanhe Ji⁶, Ken Deng², Runqing Zhang⁷,
Zhiguo Huang⁷, Ling Qian⁷, Jize Han⁷, Di Luo^{2,8*}

¹The Hong Kong University of Science and Technology (Guangzhou),
Guangzhou, China.

^{2*}Department of Physics, Tsinghua University, Beijing, China.

³School of Physics, Peking University, Beijing, China.

⁴School of Science, Sun Yat-sen University, Shenzhen, China.

⁵Shenzhen University, Shenzhen, China.

⁶Department of Physics, Southern University of Science and Technology,
Shenzhen, China.

⁷China Mobile (Suzhou) Software Technology Co., Ltd., Suzhou, China.

^{8*}Institute of Advanced Study, Tsinghua University, Beijing, China.

*Corresponding author(s). E-mail(s): diluo@tsinghua.edu.cn;

†These authors contributed equally to this work.

Abstract

Quantum control is essential for quantum information science and technology, yet designing high-fidelity control protocols remains challenging due to complex optimization landscapes, hardware noise, and long pulse sequences. Existing numerical solvers often require problem-specific engineering and produce opaque control amplitudes, while naive large language models (LLMs) lack the physical consistency and long-horizon precision for reliable quantum control synthesis. Here we introduce VF-QCTRL, a physics-informed large language model framework for general quantum control that combines symbolic reasoning with optimization to propose analytic control ansätze and coherently refine their parameters through feedback. To systematically evaluate LLM-driven quantum control, we develop QCTRL-BENCH, a benchmark spanning sixteen tasks across single- and multi-qubit systems, closed and open quantum dynamics, noiseless and noisy settings, and both analytic and numerical protocols. Across the benchmark, VF-QCTRL demonstrates strong universality, accuracy, efficiency, and interpretability: it

applies to generic quantum control systems without task-specific training, achieves performance competitive with or exceeding state-of-the-art conventional solvers in both noiseless and noisy regimes with query efficiency, exhibits favorable inference-time scaling and pulse resolution scaling, and derives physically interpretable analytical protocols directly from prompts. Our results establish physics-informed LLM-based quantum control as a promising paradigm for accurate, efficient, interpretable, and training-free quantum control protocol design across a broad range of quantum systems.

Keywords: Quantum control; Physics-informed large language models; AI-driven scientific discovery; Interpretable AI; Scientific Benchmark

Main

Quantum technologies rely fundamentally on the ability to manipulate quantum dynamics with high precision. Quantum control provides the operational foundation for preparing nonclassical states, implementing quantum gates, suppressing decoherence, and steering nonequilibrium dynamics across quantum computing, simulation, sensing, and metrology platforms [1, 2]. Recent advances in superconducting circuits, trapped ions, neutral atoms, and solid-state spin systems have significantly increased the scale and controllability of experimental devices [3–7], yet transforming these hardware advances into practical quantum advantage requires control protocols that remain accurate under realistic experimental imperfections. Designing such protocols is intrinsically difficult. Realistic quantum control tasks often involve searching over high-dimensional control parameter spaces with many coupled degrees of freedom, where pulse duration, multi-channel drives, and fine temporal discretization rapidly increase the optimization complexity. At the same time, quantum control landscapes are highly nonconvex, often containing extended plateaus and multiple local optima that hinder efficient optimization. Practical implementations further introduce finite pulse bandwidth, amplitude constraints, crosstalk, leakage outside the computational subspace, and calibration drift, such that protocols optimized for idealized models frequently degrade when deployed on real devices. Developing quantum control methods that are simultaneously accurate, robust, efficient, and physically interpretable therefore remains a central challenge in quantum science and engineering [8].

A broad range of theoretical and computational approaches has been developed to address different aspects of the quantum control problem. Analytical control theory provides valuable physical insight and, in special cases, admits elegant closed-form solutions [8]; however, such solutions rarely survive in realistic settings involving decoherence, experimental constraints, or strongly interacting many-body dynamics. Numerical optimal control frameworks, including GRAPE, Krotov, and CRAB [9–11], have achieved remarkable success in high-fidelity pulse engineering through iterative optimization of discretized control fields. Nevertheless, these methods typically rely on repeated gradient evaluations and large-scale simulations, making them computationally demanding for high-dimensional or noisy systems. Moreover, the resulting control sequences are

often represented as long arrays of amplitudes whose underlying physical structure is difficult to interpret or generalize. Alternative approaches based on reinforcement learning [12–17], evolutionary strategies [18], neural-network parameterizations [19, 20], and differentiable programming [21–23] improve flexibility and expressivity, but frequently require extensive task-specific design and training; recent tutorials and reviews consolidate this landscape [24, 25]. Despite substantial progress, it still remains open to develop a framework simultaneously achieves broad applicability across quantum platforms, strong control performance under noise, efficient optimization with limited queries, and interpretable protocol representations.

Recent progress in large language models (LLMs) suggests a new opportunity for quantum control by combining machine reasoning with physical knowledge. Modern LLMs demonstrate strong capabilities in mathematical reasoning [26], code synthesis [27], scientific problem solving [28], quantum-circuit design [29, 30], and autonomous scientific experimentation [31], indicating that they can internalize high-level physical patterns and transfer knowledge across domains. Unlike purely numerical optimizers, LLMs can naturally express symbolic structures, explain optimization strategies, and generate compact functional forms that are directly interpretable by humans. These properties make them particularly attractive for proposing physically meaningful control protocols. However, naive prompt-only deployment of LLMs remains insufficient for realistic quantum control tasks. Fine-grained pulse optimization involves continuous high-dimensional parameter spaces in which direct token-level autoregressive generation of long pulse sequences becomes increasingly unreliable as system size, control duration, and channel count grow. Consequently, while LLMs offer powerful reasoning and abstraction capabilities, they must be integrated with physics-informed design and feedback mechanisms to become practical tools for high-precision generic quantum control.

VF-QCTRL.

To address the limitations of both conventional quantum control solvers and naive prompt-only large language models (LLMs), we introduce *VibeFunction-Qcontrol* (VF-QCTRL) (see Figure 1), a physics-informed LLM framework for general quantum control. The design rests on a simple observation: LLMs possess strong high-level physical reasoning abilities, yet remain unreliable for direct high-dimensional numerical optimization. VF-QCTRL therefore separates *structural proposal* from *numerical refinement*. Instead of asking the LLM to emit long discretized pulse sequences, the model is prompted to generate compact analytic control ansätze for each control channel, expressed as symbolic functions of time with a small number of free coefficients that encode physically motivated structures such as oscillatory corrections, adiabatic ramps, Gaussian envelopes, or derivative-based compensation terms. The proposed analytic forms are then refined through a *coefficient optimizer* based on simultaneous-perturbation stochastic approximation (SPSA) [32], which optimizes the continuous coefficients using only feedback from the quantum control objective. To stabilize iterative reasoning, VF-QCTRL employs a dual-agent architecture: a *proposal agent* generates new protocol structures, and a lightweight *reflection agent* summarizes the strengths and weaknesses of previous repetitions into compact physics-guided

feedback for subsequent iterations. All generated expressions are validated through a constrained symbolic grammar and sandboxed parser before evaluation. By transforming high-dimensional pulse optimization into a search over a small number of physically meaningful parameters, VF-QCTRL mitigates the instability of token-level pulse generation while avoiding the opacity and unfavorable scaling of conventional numerical solvers. The framework is designed to achieve four key objectives for practical quantum control simultaneously: (i) universal, applying across diverse quantum control systems without task-specific training or fine-tuning; (ii) accurate, achieving performance competitive with or surpassing state-of-the-art optimization methods in both noiseless and noisy settings; (iii) efficient, exhibiting favorable query efficiency together with improved inference-time and pulse-resolution scaling relative to conventional gradient-free and LLM baselines; and (iv) interpretable, producing compact analytical control protocols that frequently recover physically meaningful or textbook solutions. The full algorithm is given in Methods, Section 3.1 (Algorithm 1).

QCTRL-Bench.

To systematically evaluate LLM-driven quantum control, we further develop *QCTRL-Bench*, to our knowledge the first structured benchmark designed specifically for quantum control synthesis rather than quantum knowledge recall, circuit compilation, or property prediction [33–38]. QCTRL-Bench is human-expert curated and inspired by frontier research scenarios, consisting of sixteen representative tasks organized along three complementary axes of complexity: system size (single- and multi-qubit), dynamical setting (closed and open), and analytical tractability (analytically solvable and purely numerical). Each task is specified through four components that together define a fully reproducible end-to-end evaluation pipeline. First, a natural-language task description provides the system Hamiltonian, target state or unitary, control channels, and physical constraints in standardized operator notation. Second, the benchmark defines the admissible control space, including total evolution time T , piecewise-constant pulse discretization, parameter bounds, and fixed physical constants such as coupling strengths, detunings, and Rabi frequencies. Third, each task includes a machine-verifiable fidelity objective, evaluated either through state overlap or gate overlap. Finally, QCTRL-Bench includes reference solutions from established control approaches, including GRAPE [9], CRAB [11], deep-learning-based controllers [19, 21], and closed-form analytical protocols where available. To probe robustness, every task is studied under both noiseless conditions ($\sigma = 0$) and calibration-noise settings ($\sigma = 0.02$), where the realized Hamiltonian is perturbed by fixed multiplicative drift offsets unknown to the optimizer. All LLM-driven methods are evaluated zero-shot on four frontier models, namely Claude Sonnet 4.5, Gemini 3.0 Flash, GPT-OSS-120B, and Qwen 3.5 Plus (two proprietary and two open-weight; full evaluation pipeline in Methods, Section 3.4). Beyond final fidelity, QCTRL-Bench measures query efficiency, robustness, scalability, and protocol interpretability, establishing a systematic evaluation platform for AI-driven quantum control and physics-informed machine learning.



Fig. 1: Visual summary of VF-QCTRL and QCTRL-Bench. (a) *VF-QCTRL framework*. Simple LLM and Hint LLM directly generate numerical pulse amplitudes, whereas VF-QCTRL provides a physics-informed large language model framework for general quantum control that combines symbolic reasoning with optimization to propose analytic control ansätze and coherently refine their parameters through feedback (b) *Universality*. Representative quantum control tasks included in QCTRL-Bench across diverse systems and dynamics. (c) *Accuracy and efficiency*. VF-QCTRL achieves higher fidelities and faster convergence than classical optimization and prompt-only LLM baselines. (d) *Interpretability*. Classical optimizers produce opaque numerical pulse arrays, while VF-QCTRL generates interpretable analytic control protocols through physics-informed reasoning. (e) *QCTRL-Bench composition*. Distribution of the sixteen benchmark tasks by system size, dynamical setting, and reference-solution type.

1 Results

We compare VF-QCTRL against two classes of baselines: (i) classical numerical controllers, including gradient-based, Fourier-based, deep-learning-based, and gradient-free pulse optimization methods, and (ii) prompt-only LLM baselines that directly generate pulse amplitudes without symbolic form proposal. The prompt-only baselines are divided into two settings: a *Simple LLM* condition that provides only the task specification together with a minimal reasoning instruction, and a more informed *Hint*

LLM condition that additionally supplies physics-aware guidance, relevant control paradigms, typical noise mechanisms, and structured feedback from previous iterations. In both settings, the LLM must directly emit one numerical amplitude per time slice and per control channel, without access to coefficient optimization or symbolic protocol refinement.

All methods are evaluated under identical environments, fidelity objectives, and noise conditions, allowing QCTRL-Bench to provide a rigorous and controlled framework for studying universality, accuracy, efficiency, robustness, and interpretability in LLM-driven quantum control.

Across QCTRL-Bench, VF-QCTRL demonstrates strong performance in accuracy, robustness, efficiency, scalability, and interpretability. In the noiseless regime ($\sigma = 0$; Section 1.1.1), VF-QCTRL matches or exceeds the strongest classical baseline on 15 of 16 tasks, while consistently outperforming prompt-only LLM baselines. Under calibration noise ($\sigma = 0.02$; Section 1.1.2), where the realized Hamiltonian differs from the nominal system, VF-QCTRL matches or surpasses the corresponding gradient-free classical baseline on all 16 tasks, including 11 strict improvements, demonstrating strong robustness against model mismatch. The framework also achieves favorable query efficiency (Section B), requiring substantially fewer evaluations than direct pulse-amplitude optimization. In addition, VF-QCTRL exhibits efficient inference-time scaling and pulse resolution scaling (Section 1.2), whereas prompt-only LLM baselines degrade significantly when generating long pulse value vectors. Finally, VF-QCTRL naturally produces interpretable control protocols and frequently derives physically meaningful analytical structures (Section 1.3), showing that physics-informed symbolic reasoning enables the framework not only to optimize quantum control accurately, but also to uncover compact and human-auditable physical mechanisms rather than merely fitting high-dimensional numerical pulse amplitudes.

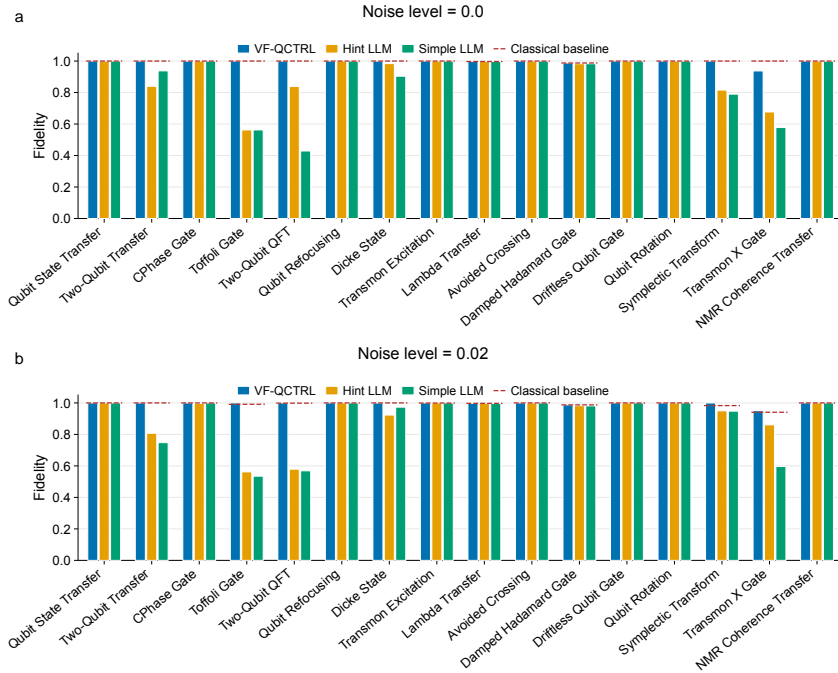


Fig. 2: Per-task best fidelity on QCTRL-Bench: VF-QCTRL versus classical and pure-LLM baselines. (a) Noiseless regime ($\sigma = 0$); the classical baseline (red dashed segment per task) is the established classical optimizer for each task (Methods, Section 3.3). (b) Calibration-noise regime ($\sigma = 0.02$); the classical baseline is exposed to the same calibration noise as VF-QCTRL. The details is documented in Methods, Section 3.4.

1.1 Accuracy and efficiency

1.1.1 Noiseless regime

Figure 2(a) summarizes the benchmark accuracy in the noiseless setting ($\sigma = 0$) across all sixteen QCTRL-Bench tasks. We compare VF-QCTRL against two classes of baselines: established classical baselines for each task reported in the literature (e.g. GRAPE, CRAB, Krylov and reinforcement learning; see Methods, Section 3.3), and two prompt-only LLM baselines, namely *Simple LLM* and *Hint LLM*.

Across the benchmark, VF-QCTRL consistently achieves high-fidelity control, reaching $F \geq 0.94$ on every task and achieving near-unit fidelity ($F \geq 0.9999$) on nine tasks (Figure 1b). Compared with classical optimization baselines, VF-QCTRL matches or approaches the strongest classical result on 15 out of 16 tasks, with only Transmon Logical X Gate approximately 0.0 lower relative to GRAPE. Notably, the advantage of VF-QCTRL becomes most apparent on difficult multi-qubit and high-dimensional tasks. For example, on Toffoli Gate Synthesis and Two-Qubit Fourier Gate Synthesis, VF-QCTRL maintains fidelities above 0.999 by proposing compact

physically meaningful ansätze, such as layered pulse structures or cosine-envelope protocols, which are subsequently refined by coefficient optimization.

In contrast, the prompt-only LLM baselines degrade substantially as task complexity increases. While both Simple LLM and Hint LLM can solve relatively simple tasks with high fidelity, their performance deteriorates on more challenging settings, including Two-Qubit Fourier Gate Synthesis, Toffoli Gate Synthesis, Coupled-Oscillator Symplectic Transform, and Transmon Logical X Gate, where the fidelity gap can reach nearly 0.6. Although Hint LLM consistently improves over Simple LLM by incorporating physics-aware guidance and iterative feedback, both baselines remain fundamentally limited by the difficulty of directly generating long numerical pulse vectors. These results demonstrate that the advantage of VF-QCTRL arises not merely from providing physics hints to the model, but from enabling symbolic control-form proposal combined with efficient coefficient refinement. Furthermore, VF-QCTRL provides interpretable formula for quantum control protocol, which will be presented in Section 1.3.

1.1.2 Noisy regime

To evaluate robustness under realistic hardware imperfections, we study all QCTRL-Bench tasks in a calibration-noise setting with $\sigma = 0.02$, where the drift Hamiltonian is perturbed by fixed multiplicative offsets applied independently to task-specific physical parameters such as Rabi frequencies, couplings, and energy gaps:

$$p_{\text{noisy}} = p(1 + \delta_p), \quad \delta_p \in \{-\sigma, +\sigma\}, \quad \sigma = 0.02. \quad (1)$$

The perturbation remains fixed throughout each optimization repetition, corresponding to static miscalibration rather than stochastic shot noise. Importantly, each method only knows the nominal Hamiltonian and has no direct access to the perturbed parameters or the value of σ . VF-QCTRL adapts to the noisy environment indirectly through iterative feedback. At each round, the proposal agent generates a compact analytic protocol, while the resulting fidelity under the perturbed Hamiltonian is returned through the rolling feedback memory together with the rendered control form. The reflection agent then summarizes useful physical patterns and failure modes from previous repetitions, allowing subsequent proposals to progressively adapt to the effective noisy dynamics despite never explicitly observing the calibration offsets.

Figure 2(b) reports per-task best fidelity at the calibration noise $\sigma = 0.02$: Across all sixteen tasks, VF-QCTRL matches or exceeds the classical baseline, achieving 11 strict improvements while remaining within 0.001 fidelity on the remaining tasks, and exceeding the two prompt-only LLM baselines on every multi-qubit and high-dimensional task. The advantage comes from searching a low-dimensional symbolic ansatz rather than a flat $\mathcal{O}(N_t \cdot C)$ -dimensional amplitude vector (N_t piecewise-constant time slices, C independent control channels), so VF-QCTRL is more drift-robust than the classical baseline and more reliable than naive amplitude generation. The largest gains over the classical baseline are on Dissipative Lambda Transfer ($F = 0.997$ vs. 0.966 , $\Delta F = +0.031$), Coupled-Oscillator Symplectic Transform (0.9997 vs. 0.983 , $+0.017$), Transmon Logical X Gate (0.950 vs. 0.941 , $+0.010$), and Toffoli Gate Synthesis (0.9996 vs. 0.991 , $+0.008$); Transmon Logical X Gate is particularly informative because

in the noiseless regime it was the worst VF-QCTRL task, trailing GRAPE by 0.06 in fidelity, yet under miscalibration the symbolic ansatz now wins, since a few-coefficient analytic form absorbs drift that a full amplitude search cannot. VF-QCTRL’s fidelity advantage over the prompt-only baselines is largest on multi-qubit and high-dimensional tasks: on Two-Qubit Fourier Gate Synthesis and Toffoli Gate Synthesis, Simple LLM and Hint LLM cluster at $F \approx 0.53$ – 0.58 while VF-QCTRL stays above $F = 0.999$; on Two-Qubit State Transfer they reach only $F \approx 0.74$ – 0.80 versus VF-QCTRL’s $F = 1.000$; on shorter single-qubit tasks and Avoided-Crossing State Transfer they remain competitive, because direct numerical pulse generation is stable when the pulse sequence is short.

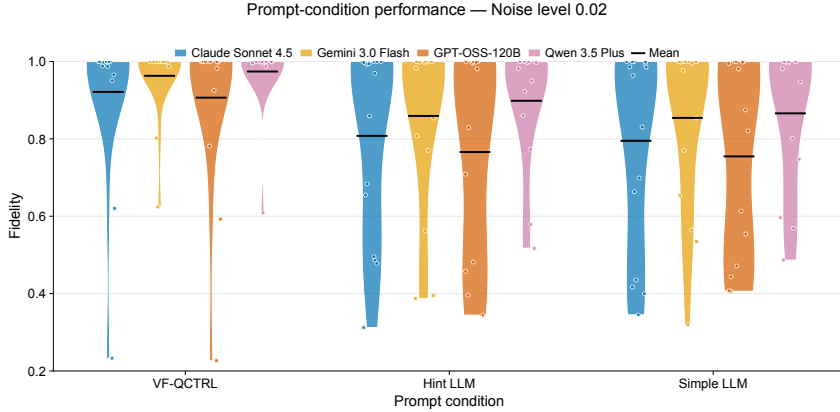


Fig. 3: Distribution of per-task best fidelity at $\sigma = 0.02$ across LLM-driven methods. Each violin shows the 16 per-task best fidelities for one (model, method) cell: four models (Claude Sonnet 4.5, Gemini 3.0 Flash, GPT-OSS-120B, Qwen 3.5 Plus) \times three methods (VF-QCTRL, Hint LLM, Simple LLM), giving 12 violins. Per-task fidelity convention: for VF-QCTRL, the best-of-iteration value from a single repetition per task ($n = 1$); for Hint LLM and Simple LLM, the best across $n = 5$ independent repetitions per task. Overlaid scatter points show the 16 individual per-task fidelities; the horizontal black tick inside each violin marks the mean. VF-QCTRL violins concentrate near $F = 1$ across all four models; Hint LLM and Simple LLM violins are broader and run longer low-fidelity tails. The $\sigma = 0$ case is shown in Figure 8.

Figure 3 stratifies the same $\sigma = 0.02$ results by the underlying LLM, showing per-task fidelity distributions for each (method, model) cell. VF-QCTRL violins concentrate near $F = 1$ with per-model mean fidelity in the 0.91–0.98 range across all four models, while Hint LLM and Simple LLM violins broaden into long low-fidelity tails reaching $F \approx 0.3$ – 0.5 with per-model means dropping to 0.75–0.90; symbolic protocol proposal thus compresses the cross-model spread from approximately 0.12 in fidelity under the prompt-only baselines to 0.06 under VF-QCTRL. Across all three methods the four LLMs rank consistently as Qwen 3.5 Plus > Gemini 3.0 Flash > Claude Sonnet 4.5 > GPT-OSS-120B, but VF-QCTRL absorbs most of this cross-model capability gap:

the weakest model under VF-QCTRL (GPT-OSS-120B, mean $F = 0.91$) matches the strongest model under Hint LLM (Qwen 3.5 Plus, mean $F = 0.90$). The low-fidelity tails of the prompt-only methods are heaviest on Claude Sonnet 4.5 and GPT-OSS-120B and are driven by the same multi-qubit tasks (Two-Qubit Fourier Gate Synthesis, Toffoli Gate Synthesis) that fail in Figure 2(b).

Beyond final fidelity, VF-QCTRL is more efficient than the baselines in both iterations and language-model tokens. Under calibration noise ($\sigma = 0.02$), VF-QCTRL reaches $F = 0.999$ in fewer iterations than the classical baseline on tasks that admit a compact analytical form (Figures 6), and consumes fewer or comparable LLM tokens than both prompt-only baselines (Hint LLM and Simple LLM) across all four evaluated models (Figure 7). Per-task and per-model breakdowns are given in Appendix B.

1.2 Inference-time and pulse-resolution scaling

Inference-time scaling and pulse-resolution scaling provide two complementary perspectives on the behavior of VF-QCTRL. The first examines how performance improves as the framework is allowed more independent proposal-reflection repetitions, probing whether additional reasoning cycles can continue to refine control quality. The second studies how performance changes as the number of piecewise-constant time slices increases, which directly tests whether the framework remains stable in high-dimensional control settings. Together, these scaling tasks highlight a key distinction between VF-QCTRL and prompt-only LLM approaches: VF-QCTRL operates through compact symbolic control representations whose complexity remains largely independent of pulse discretization, whereas naive LLM baselines must directly generate increasingly long numerical pulse vectors as the control resolution grows.

Figure 4(a–b) shows the *inference-time scaling* behavior of VF-QCTRL under calibration noise ($\sigma = 0.02$) on representative tasks including Dicke State Preparation and Transmon Logical X Gate. On both tasks the running-best infidelity decreases in discrete stepwise drops as the number of independent repetitions n increases, reflecting the progressive discovery of better control ansätze across repetitions. Dicke State Preparation descends to infidelities on the order of 10^{-4} , while Transmon Logical X Gate plateaus near 10^{-2} ; in both cases, additional repetitions continue to deliver fidelity improvements rather than stalling at the first solution. Overall, the observed trend demonstrates that VF-QCTRL benefits naturally from increased inference-time compute through iterative reasoning and protocol refinement rather than relying solely on larger pretrained model capacity.

Figure 4(c–d) presents the *pulse-resolution scaling* results as the number of time slices increases from $N_t = 20$ to $N_t = 220$. VF-QCTRL maintains consistently strong fidelities across all tested resolutions, with only modest variation as the discretization grid becomes finer. In contrast, both Simple LLM and Hint LLM baselines deteriorate rapidly with increasing N_t , particularly at high resolutions where the models must generate extremely long numerical pulse sequences directly. At $N_t = 220$, the fidelities of the prompt-only baselines fall below 0.4 on representative tasks, whereas VF-QCTRL remains stable. This difference arises because VF-QCTRL searches over compact analytic control forms whose effective complexity remains nearly independent of the pulse grid, while prompt-only methods scale directly with the length of the numerical

control vector. These results identify pulse-resolution scaling as a central advantage of symbolic protocol proposal and demonstrate that VF-QCTRL can remain effective in regimes where direct high resolution pulse generation becomes unstable.

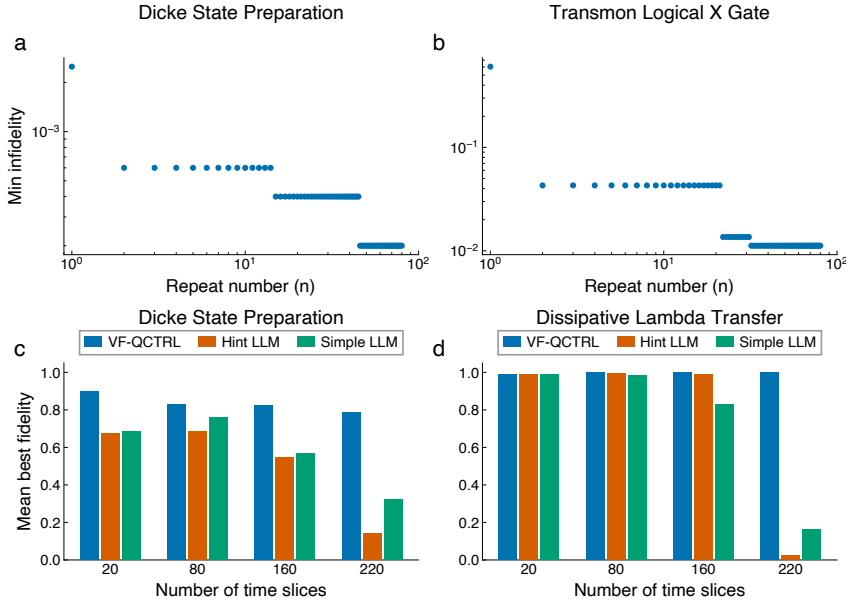


Fig. 4: Scaling diagnostics. (a, b) VF-QCTRL running-minimum infidelity $\epsilon_n = \min_{i \leq n} (1 - F_i)$ versus the number of independent repetitions n . On both tasks the running-minimum infidelity decreases with n , reaching $\sim 10^{-4}$ for Dicke State Preparation and $\sim 10^{-2}$ for Transmon Logical X Gate. (c, d) Mean best fidelity plotted against the number of piecewise-constant time slices. For both Dicke State Preparation and Dissipative Lambda Transfer tasks, VF-QCTRL maintains high fidelity while pure LLM methods deteriorate rapidly with increasing N_t . All tasks in the figures are performed under calibration noise $\sigma = 0.02$.

1.3 Interpretability

Beyond final performance, VF-QCTRL offers interpretability at two distinct levels: (i) *Formula-Level Interpretability*, as it returns explicit, compact functional expressions instead of opaque numerical pulse arrays; and (ii) *Reasoning-Level Interpretability*, since it exposes the LLM’s step-by-step reasoning trace explaining how those expressions were chosen and physically derived. We can therefore inspect not only whether the proposed controls correspond to valid physical mechanisms, but also whether the model’s intermediate reasoning reflects the correct underlying physics. To understand the LLM’s contribution, we analyze two tasks from VF-QCTRL with zero-step coefficient-optimizer, where the LLM proposes both the functional form and its initial coefficients

directly, with no subsequent numerical refinement. We note that these tasks are curated such that their exact setup has not appeared in the literature, and the closed-form references are never exposed to the model; the prompt provides only the Hamiltonian, available controls, objective, and time discretization. As illustrated in Fig. 5, even without parameter optimization, VF-QCTRL protocols achieve high physical fidelity by deriving the correct mathematical structures.

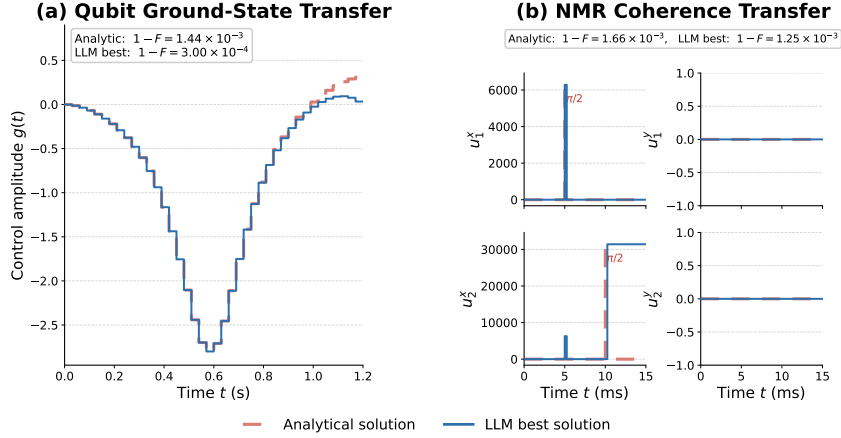


Fig. 5: Analytical structure in VF-QCTRL outputs at noiseless regime. (a) Qubit Ground-State Transfer: the LLM derives the continuous-time CD control law and identifies discretization-dependent corrections. (b) NMR Coherence Transfer: the LLM utilizes the product-operator evolution to derive four control pulses with high fidelity.

The first case is Qubit Ground-State Transfer, evaluated on Qwen 3.5 Plus. In this task, the goal is to steer a spin-1/2 particle along its instantaneous ground state under a time-dependent qubit Hamiltonian:

$$H_{\text{total}}(t) = 1.0 \times (1 + (t/1.2)^3) \sigma_x + (2.0 - 4.0 \times S(t/1.2)) \sigma_z - g(t) \sigma_y \quad (2)$$

where $S(\tau) = 10\tau^3 - 15\tau^4 + 6\tau^5$ is a quintic smoothstep function, and the cubic transverse (i.e., $1.0 \times (1 + (t/1.2)^3)$) and smoothstep longitudinal (i.e., $2.0 - 4.0 \times S(t/1.2)$) sweeps form a custom configuration designed specifically for this benchmark that has not appeared in prior literature. The control $g(t)$ is discretized into 40 slices over $T = 1.2$.

LLM-derived formula. The LLM actively recognizes the control channel coefficients in $H_{\text{total}}(t)$ to derive the continuous-time counter-diabatic field, introducing $\Omega_x(t)$ and $\Omega_z(t)$ as the coefficients of the Pauli operators σ_x and σ_z :

$$g(t) = \frac{\Omega_x \dot{\Omega}_z - \Omega_z \dot{\Omega}_x}{2(\Omega_x^2 + \Omega_z^2)}.$$

As shown in Fig. 5(a), this derived formula is closely aligned with the analytical counter-diabatic driving protocol. Indeed, the LLM further introduced small correction terms on top of the counter-diabatic term in an attempt to compensate for errors introduced by temporal discretization, achieving higher fidelity state preparation than the normal CD driving protocol without any parameter optimization.

LLM reasoning. The LLM’s reasoning trace (see Appendix D.1 for the verbatim trace) demonstrates clear physical intuition by mapping the drifting qubit Hamiltonian (the uncontrolled terms along σ_x and σ_z in Eq. (2): $H_0(t) = 1.0 \times (1 + (t/1.2)^3) \sigma_x + (2.0 - 4.0 \times S(t/1.2)) \sigma_z$) to a spin-1/2 particle in an effective magnetic field $\vec{B}_0(t) = (\Omega_x(t), 0, \Omega_z(t))$. For instance, it derives: “The CD term for a spin in a magnetic field $B_0(t)$ is $H_{\text{CD}} = (B_0 \times \dot{B}_0)/(2|B_0|^2)$ ”. Furthermore, it actively diagnoses and identifies the temporal discretization effects introduced by the finite time grid ($N_t = 40$), pointing out in its reasoning trace that the “Midpoint rule is 2nd order” (implying the global simulation error of the time-ordered propagator scales as $\mathcal{O}(\Delta t^2)$) and explaining the physical reason why the discrete sequence of rotations fails to perfectly track the continuous-time analytical CD drive (e.g., “In discrete time, the ‘kick’ from $H(t_k)$ is exact for that slice, but the sequence of rotations doesn’t perfectly track”).

NMR Coherence Transfer provides a sequence-level example, evaluated on Qwen 3.5 Plus. This task considers polarization transfer between two weakly coupled spin-1/2 particles (labeled 1 and 2) under a J-coupling Hamiltonian:

$$H(t) = 2\pi JS_1^z S_2^z + u_1^x(t)S_1^x + u_1^y(t)S_1^y + u_2^x(t)S_2^x + u_2^y(t)S_2^y \quad (3)$$

where $J = 100$ Hz, over a total duration $T = 15.0$ ms discretized into exactly 60 time slices ($\Delta t = 0.25$ ms).

LLM-derived formula. The LLM reasons that the coupling term $2\pi JS_1^z S_2^z$ generates anti-phase coherence, and utilizes the analytic product-operator evolution under this term for duration τ :

$$S_2^x \xrightarrow{2\pi JS_1^z S_2^z \tau} S_2^x \cos(\pi J\tau) + 2S_1^z S_2^y \sin(\pi J\tau). \quad (4)$$

To maximize the transfer from the single-spin coherence S_2^x to the anti-phase coherence $2S_1^z S_2^y$ (the second term in Eq. (4)), the model targets a state where $\sin(\pi J\tau) = 1$ and $\cos(\pi J\tau) = 0$. Based on this relation, the model analytically derives the optimal delay time $\tau = 1/(2J) = 5$ ms (for $J = 100$ Hz), yielding a precise sequence-level control strategy. To translate this into continuous control fields, the LLM proposes Heaviside-based rectangular pulses along the x -direction channels $u_1^x(t)$ and $u_2^x(t)$ (in rad/s) while setting $u_1^y(t) = u_2^y(t) = 0$ since no y -axis rotations are required for this sequence. Specifically, after the initial 5 ms delay, it applies simultaneous $\pi/2$ pulses of opposite signs (amplitude $-2\pi \times 10^3$ rad/s on particle 1 to rotate $S_1^z \rightarrow -S_1^z$, and $2\pi \times 10^3$ rad/s on particle 2 to rotate $S_2^y \rightarrow S_2^z$) over 0.25 ms, yielding the exact pulse area of $\pi/2$ rad for phase-coherent transfer $2S_1^z S_2^y \rightarrow -2S_1^y S_2^z$. Following a second 5 ms delay to obtain target S_1^x at $t = 10.25$ ms, the model addresses the remaining simulation time by applying a strong continuous-wave decoupling field ($2\pi \times 5 \times 10^3$ rad/s $\gg 2\pi J$) on $u_2^x(t)$ from 10.25 to 15.0 ms. This spin-locks the second particle ($\langle S_2^z \rangle \approx 0$), effectively

suppressing the coupling interaction and freezing the target state at high fidelity, as shown in Fig. 5(b).

LLM reasoning. The LLM’s reasoning trace (see Appendix D.2 for the verbatim trace) illustrates how it maps the continuous-time physical process to the discrete simulation grid while acknowledging the limits of physical approximations. The LLM identifies the problem as “coherence transfer via scalar coupling” and constructs the ideal switching sequence (free evolution, phase-appropriate local $\pi/2$ rotations, and a second free-evolution interval). It then translates this to the temporal discretization, mapping the analytical delay $\tau = 5$ ms to exactly 20 time slices of $\Delta t = 0.25$ ms, demonstrating its capacity to perform temporal discretization mapping. It further recognizes that finite-width pulses are imperfect from the delta pulse because “During the pulse, J-coupling is also active”, introducing side effects from the other term. It also explicitly reasons about how to freeze the target state during the remaining 4.75 ms of the simulation, writing: “We need to preserve I_x from 10.25 to 15.0. Apply CW decoupling on S ($u_{Sx} = \text{large}$). This averages $I_z S_z$ to 0 (in the frame of S). Actually, if we lock S along x, $I_x = 0$. So $I_z S_z$ averages to 0. I_x is stable.” (here the LLM’s symbols I and S map to particle 1 and particle 2 in our notation, so that I_x , u_{Sx} , and $I_z S_z$ correspond to S_1^x , u_2^x , and $S_1^z S_2^z$, respectively).

Together, these examples show that interpretability lies in the derivational structure of the solution, not merely in the final pulse representation. In Qubit Ground-State Transfer, the LLM derives a continuous-time CD control law. In NMR Coherence Transfer, it derives an analytical sequence-level mechanism. This hierarchy of formula-level and reasoning-level interpretability is precisely what is lost in raw GRAPE or CRAB amplitude arrays: the numerical pulse may be accurate, but the mechanism is not explicitly named, derived, or checked against the physics.

2 Discussion

In this work, we introduced *VF-QCTRL*, a physics-informed large language model framework for general quantum control that combines symbolic protocol proposal with iterative physics-guided optimization. Rather than directly generating high-dimensional numerical pulse sequences, VF-QCTRL enables the LLM to propose compact analytic control forms that encode physical structure and reasoning, while the feedback iteratively refines the resulting protocols. To systematically evaluate this setting, we further developed *QCTRL-Bench*, a sixteen-task benchmark spanning single- and multi-qubit systems, closed- and open-system dynamics, noiseless and calibration-noise regimes, as well as analytical and fully numerical control problems. Across the benchmark, VF-QCTRL demonstrates strong universality, accuracy, efficiency, scalability, and interpretability. The framework matches or exceeds the classical baselines on nearly all noiseless tasks and consistently maintains strong performance under calibration noise, while significantly outperforming prompt-only LLM baselines. In addition, VF-QCTRL exhibits favorable query efficiency, robust inference-time and pulse-resolution scaling behavior, and the ability to derive interpretable analytical control structures directly from task descriptions. Together, these results establish physics-informed large language

models that integrates symbolic reasoning and numerical optimizer as a promising paradigm for AI-driven quantum control.

Several important directions remain for future work. On the algorithmic side, future improvements include incorporating more expressive symbolic grammars, adaptive allocation of proposal-reflection budgets across optimization stages, and retrieval-augmented physics guidance that dynamically selects relevant control paradigms without prompt engineering. An especially important next step is deployment on real quantum hardware. Since VF-QCTRL is able to operate through iterative feedback rather than requiring differentiable models, the framework naturally interfaces with hardware-in-the-loop optimization settings. This opens the possibility of directly applying VF-QCTRL to superconducting quantum processors, neutral-atom arrays, trapped-ion systems, and other programmable quantum platforms subject to calibration drift, analog bandwidth constraints, crosstalk, and device-specific noise. More broadly, VF-QCTRL suggests a path toward integrating scientific reasoning, symbolic structure design, and numerical optimization within a unified agentic framework for scientific machine learning. Extending these ideas to larger many-body quantum systems, hardware-aware optimal control, and autonomous experiment design represents an important opportunity for future research.

3 Methods

This section defines VF-QCTRL as a control-synthesis method (Section 3.1), describes the QCTRL-Bench task suite used to evaluate it (Section 3.2), the classical and pure-LLM baselines we compare against (Section 3.3), and the evaluation pipeline and metrics (Section 3.4). The full task descriptions are given in Appendix A.

3.1 The VF-QCTRL algorithm

VF-QCTRL is a physics-informed LLM-based quantum control framework designed around the complementary strengths and weaknesses of large language models. While LLMs possess strong high-level physical reasoning and pattern abstraction abilities, they are unreliable for direct high-dimensional numerical optimization. VF-QCTRL therefore assigns the LLM a structural role: instead of generating discretized pulse amplitudes directly, the model is asked to propose compact analytic control ansätze for each control channel, consisting of symbolic functions of time with a small number of freely varying coefficients. The pipeline is organized as a dual-agent iterative optimization loop with three components acting in sequence at each round. A *proposal agent* generates, for every control channel, a parameterized analytic ansatz together with initial coefficient values. A *coefficient optimizer* then numerically refines those coefficients against a fidelity oracle using a gradient-free black-box algorithm; throughout this work we use Spall’s simultaneous-perturbation stochastic approximation (SPSA) [32] for its sample-efficiency, although the framework is compatible with other gradient-free optimizers. Finally, a *reflection agent* distills the round’s reasoning trace and observed fidelity into a compact summary that is fed back into the next round’s proposal agent. The loop terminates once the optimized infidelity falls below a target tolerance ε or the outer-loop budget K is exhausted.

The proposal agent reads a structured prompt with three components: (i) a task specification containing the Hamiltonian, control channels, optimization target, physical constraints, and fidelity tolerance; (ii) a physics-guidance block summarizing relevant control paradigms and reminding the model of potential calibration noise or Hamiltonian mismatch; and (iii) a rolling feedback memory, written by the reflection agent, containing selected previous repetitions together with their analytic forms, optimized infidelities, and summaries of why particular strategies succeeded or failed. The first iteration is initialized from a zero-amplitude warm start with an empty feedback memory and asks the model to propose control structures from scratch. At each iteration k , the agent outputs, for each control channel, a structured representation

$$\{\text{expression: } s_c, \text{ parameters: } \{a_1:\theta_1^{(0)}, \dots, a_p:\theta_p^{(0)}\}\},$$

where s_c is a symbolic expression in time t , total duration T , and trainable parameters $\{a_i\}$, and $\{\theta_i^{(0)}\}$ are the agent’s proposed initial values. To ensure robustness and physical interpretability, the symbolic grammar is intentionally constrained: only the operations $+$, $-$, \times , $/$, \wedge and the functions \sin , \cos , \exp , \log , erf , \tanh , sinc , Θ are permitted, with at most $p = 60$ freely varying coefficients and being non-zero. For example, on a Landau–Zener task the agent may propose a monotonic sweep supplemented by a corrective oscillatory term, whereas for a DRAG-style protocol it may generate a Gaussian envelope together with derivative compensation. Crucially, the agent proposes only the functional structure and reasonable initial coefficient values; all numerical refinement is handled by the coefficient optimizer. This constrained symbolic representation lets VF-QCTRL search efficiently over physically meaningful protocol families rather than unrestricted numerical pulse spaces.

The coefficient optimizer uses SPSA because it requires only two objective evaluations per optimization step regardless of the parameter dimension p . The update rule is

$$\begin{aligned} \Delta_k &\sim \text{Rademacher}(\{-1, +1\})^p, & y_{\pm} &= J(\theta_k \pm c_k \Delta_k), \\ \hat{g}_k &= \frac{y_+ - y_-}{2c_k} \Delta_k, & \theta_{k+1} &= \text{clip}(\theta_k - a_k \hat{g}_k), \end{aligned} \tag{5}$$

with gain schedules $a_k = a/(k + 1 + A)^{0.602}$ and $c_k = c/(k + 1)^{0.101}$ following the standard SPSA prescription ($A = 50$; a and c are task-dependent hyperparameters). The objective is $J(\theta) = 1 - F(\theta)$: at each evaluation, the proposed analytic expression is discretized on the midpoint time grid, converted into a piecewise-constant control sequence, and evaluated by a *fidelity oracle*. In this work the fidelity oracle is a quantum simulator, but it is treated as a black-box evaluator, so the same optimizer applies uniformly across closed-system unitary evolution, Lindbladian open-system dynamics, noisy calibration models, and, in principle, a fidelity estimator running on real hardware. The optimizer runs for at most B_{opt} steps per round (default 10^3) and returns the refined infidelity $1 - F_k$ together with the rendered analytic protocol obtained by substituting the optimized coefficients into the symbolic expression.

Between rounds, the reflection agent analyzes the previous proposal and its observed fidelity improvement $F_k - F_{k-1}$ and emits a compact set of feedback bullets that preserve useful physical reasoning while avoiding prohibitively long reasoning traces.

Algorithm 1 VF-QCTRL control synthesis framework.

Require: Quantum control task \mathcal{T} ; physics-informed skill h ; proposal agent π ; reflection agent π' ; outer-loop budget K ; coefficient-optimization budget B_{opt} ; target tolerance ε .

Ensure: Best analytic protocol (s^*, θ^*) and optimized infidelity $1 - F^*$.

```
1:  $\mathcal{H} \leftarrow \emptyset$ ;  $F^* \leftarrow 0$  ▷ rolling feedback memory and best fidelity
2: for  $k = 1, 2, \dots, K$  do
3:    $P_k \leftarrow \text{BUILD\_PROMPT}(\mathcal{T}, h, \mathcal{H})$ 
4:    $\{s_c, \theta_c^{(0)}\}_c \leftarrow \pi(P_k)$  ▷ proposal agent generates analytic forms and initial coefficients
5:   validate symbolic expressions  $s \leftarrow \{s_c\}_c$  against the constrained grammar
6:    $(\theta_k^*, F_k) \leftarrow \text{OPTIMIZE}(\theta \mapsto 1 - F(\mathcal{T}, s(\theta)), \theta^{(0)}, B_{\text{opt}})$  ▷ gradient-free coefficient refinement using Eq. (5)
7:   append  $(s, \theta_k^*, F_k, \text{rendered form})$  to  $\mathcal{H}$ 
8:   update  $F^*$  and  $(s^*, \theta^*)$ 
9:   if  $k \geq 2$  then
10:     $r_k \leftarrow \pi'(\text{reasoning}_{k-1}, F_k - F_{k-1})$  ▷ reflection agent summarizes useful physical insights
11:    append  $r_k$  to  $\mathcal{H}$ 
12:   end if
13:   if  $1 - F_k \leq \varepsilon$  then
14:     break ▷ target fidelity achieved
15:   end if
16: end for
17: return  $(s^*, \theta^*, 1 - F^*)$ 
```

These bullets, together with that round’s analytic form, optimized infidelity, and rendered protocol, are appended to the rolling feedback memory and consumed by the proposal agent in the next iteration. The proposal agent may then either refine the same functional basis or mutate the structure itself by introducing additional oscillatory terms, phase shifts, Gaussian corrections, or alternative basis functions, evolving protocol structures based on distilled physical insight rather than raw numerical amplitudes. This mechanism lets the LLM focus on proposing meaningful structural changes (oscillatory corrections for adiabatic sweeps, derivative compensation for leakage suppression, counter-intuitive pulse ordering in STIRAP-like dynamics), while numerical refinement is handled separately by the coefficient optimizer. The outer loop runs for at most K iterations (default 50) or until the target tolerance ε is reached; the complete VF-QCTRL pipeline is summarized in Algorithm 1.

3.2 QCTRL-Bench

QCTRL-Bench is a sixteen-task suite organized along three orthogonal axes of difficulty (system size, dynamical setting, and analytical tractability), whose per-axis task counts are summarized in Figure 1(e). Full per-task specifications are in Appendix A. Each

task is defined by four components, together sufficient to drive the evaluation pipeline of Section 3.4 end-to-end:

(i) a *natural-language specification*: the system Hamiltonian in standard operator notation with LaTeX markup for precise parsing, the initial and target states or unitaries, the control parameterization, and any physical constraints;

(ii) a *control space*: the number of piecewise-constant time slices and total evolution time T , field bounds (e.g. phase angles $\alpha \in [-\pi, \pi]$, detuning $\nu \in [\nu_{\min}, \nu_{\max}]$, depending on the system), fixed physical parameters (Rabi frequency Ω , coupling J , drift coefficients, energy gap Δ), and the number and type of independent control channels;

(iii) a *machine-verifiable fidelity objective* with target tolerance ε : either a state-overlap or a gate-overlap on a Hilbert space of dimension d ,

$$F_{\text{state}} = |\langle \psi_{\text{target}} | \psi(T) \rangle|^2, \quad F_{\text{gate}}(U_{\text{target}}, U) = \frac{1}{d^2} |\text{Tr}(U_{\text{target}}^\dagger U)|^2; \quad (6)$$

and

(iv) a *classical baseline fidelity*: a precomputed fidelity from GRAPE (numerical-only tasks), CRAB (frequency-tuned tasks), or the closed-form protocol (the seven analytically tractable tasks), used only as a comparison target in the Results. For the seven analytically tractable tasks, the closed-form protocol additionally serves as the interpretability anchor of Section 1.3 and is never exposed to the LLM. Scoring is defined entirely by (iii); the LLM sees only (i) and (ii), plus a zero-amplitude warm-start with its computed fidelity at iteration $k = 1$ for VF-QCTRL (Section 3.1).

Calibration noise. Each task is evaluated under two conditions: a noiseless baseline ($\sigma = 0$) and a miscalibrated drift Hamiltonian ($\sigma = 0.02$). In the miscalibrated condition, at the start of each outer-loop run every drift parameter p receives a fixed multiplicative offset $p \rightarrow p(1 + \delta_p)$ with $\delta_p \in \{-\sigma, +\sigma\}$ chosen once, independently per parameter, and held constant for the entire coefficient-optimization loop and for every subsequent evaluation within that run (static miscalibration, not shot noise). The LLM sees only the nominal parameters, so the $\sigma = 0.02$ condition tests whether a protocol remains high-fidelity when the true Hamiltonian differs from the one it was designed against—the regime in which real hardware always operates.

3.3 Baselines

We compare VF-QCTRL against two structurally different families of alternative. *Classical numerical controllers* (GRAPE, CRAB, deep-learning optimizers, and gradient-free pulse-amplitude optimization) act as an *external reference*: they fix the floor and ceiling of attainable fidelity on each task and are precomputed once with the benchmark. *Prompt-only LLM baselines* (Simple LLM and Hint LLM) act as an *ablation of the form-proposal step*: they share VF-QCTRL’s outer-loop scaffolding but the model must emit numerical amplitudes directly, bypassing form proposal. Both families are run under the same noise model and against the same fidelity objective as VF-QCTRL, so any gap is attributable to the method rather than to the evaluation protocol.

For each task, the classical baseline is derived from the chosen optimizer used in the prior literature that originally introduced or studied that task. Under zero noise,

all 16 tasks in A uses one of the three choices: GRAPE [9] (gradient-based, L-BFGS-B) for numerical-only tasks, CRAB [11] (Fourier-basis, Nelder–Mead) for frequency-tuned tasks, and the closed-form analytical protocol for analytically tractable tasks. Under noise level, $\sigma = 0.02$, the classical baseline is a Chopped Random Basis (CRAB) pulse optimized via the SPSA algorithm (CRAB+SPSA), which is chosen as a standard robust gradient-free method for pulse optimization under calibration noise. Specifically, the control field for each channel c is parameterized multiplicatively as $u_c(t) = u_{0,c}(t)(1 + f_c(t))$, where $u_{0,c}(t)$ is the initial control guess (either a random initialization or a GRAPE solution of the noise-free problem), and $f_c(t) = \sum_{k=1}^m [A_{c,k} \sin(\omega_{c,k}t) + B_{c,k} \cos(\omega_{c,k}t)]$ (where $m = 20$) is a chopped random basis modulation signal with randomized frequencies $\omega_{c,k}$ and optimized coefficients $\{A_{c,k}, B_{c,k}\}$. SPSA (following the same update rule of Eq. (5)) is then applied directly to optimize the coefficients $\{A_{c,k}, B_{c,k}\}$ under calibration noise, exposed to the same noise as VF-QCTRL.

Both pure-LLM baselines share VF-QCTRL’s outer-loop budget K but remove the coefficient optimizer entirely: the model must emit numerical amplitudes directly. The two conditions differ in both the physics hint and whether structured feedback is returned between iterations:

- *Simple LLM*: a minimal hint consisting of the single injunction “Think!”, with no physics context beyond the task specification and no reflection-agent feedback between iterations.
- *Hint LLM*: a physics-aware hint that names relevant control paradigms and lists typical noise sources. The full text of the hint is reproduced verbatim in Appendix C.1. The reflection-agent feedback block carried from previous iterations.

In both baselines, the LLM writes the pulse out directly as a list of numerical amplitudes rather than as an analytic formula in VF-QCTRL methods. The fidelity is calculated from the proposed optimized coefficients.

3.4 Evaluation pipeline and metrics

Each *control task* runs through a four-phase pipeline for LLM approaches (Figure 1(d)):

- *Prompt assembly*: packages the task specification (Hamiltonian, initial and target states, control parameterization, constraints) into a single prompt. For VF-QCTRL and Hint LLM, a rolling memory of previous rounds (prior proposals and reflection notes) is also appended.
- *Pulse proposal*: sends the prompt to the LLM and parses its reply. VF-QCTRL receives a short analytic expression per control channel (for example, $f(t) = \Omega \sin(\omega t)$ with a few free coefficients), which the coefficient optimizer then tunes against the simulator for up to $B_{\text{opt}} = 10^3$ steps; Simple LLM and Hint LLM receive a list of pulse amplitudes, one per time slice, taken as-is.
- *Fidelity evaluation*: computes the quantum dynamics under the (possibly noisy) controls and computes the task fidelity.
- *Reflection*: closes the round. For VF-QCTRL and Hint LLM, a separate reflection agent summarizes the round into bullets that are appended to the next round’s

prompt; Simple LLM has no reflection information and starts each round from the unchanged task prompt.

Rounds repeat until $1 - F^* \leq \varepsilon$ or the outer-loop budget $K = 50$ is reached. Classical baselines are precomputed once per task outside this pipeline (Section 3.3). The pipeline is built on the SDE-Harness [39] workflow engine with a LiteLLM [40] provider layer.

Four frontier LLMs are evaluated across all applicable methods: Claude Sonnet 4.5, Gemini 3.0 Flash, GPT-OSS-120B, and Qwen 3.5 Plus. We report three metrics: the *task fidelity* F ; the *token efficiency* (output tokens per repetition); and the *iteration efficiency* (outer-loop iterations to reach tolerance, capped at $K = 50$).

We use $n = 1$ repetition for VF-QCTRL and $n = 5$ repetitions for Simple LLM and Hint LLM (reporting the best repetition over the five). The corresponding per-model fidelity distributions are reported in Figure 3 ($\sigma = 0.02$, main text) and Figure 8 ($\sigma = 0$, Appendix).

3.5 Scaling-study protocols

The two scaling control tasks in Figure 4 use sampling protocols that differ from the main-text benchmark. All scaling experiments use Claude Sonnet 4.5 as the underlying LLM. For the inference-time scaling panels (a, b), each task runs for $n = 80$ independent VF-QCTRL repetitions with distinct random seeds, in contrast to the main-text per-task convention of $n = 1$ VF-QCTRL repetition. For the pulse-resolution scaling panels (c, d), each task uses $n = 1$ VF-QCTRL repetition and $n = 5$ repetitions per pure-LLM baseline, but at four pulse-resolution settings $N \in \{20, 80, 160, 220\}$.

Acknowledgments

DL acknowledges support from Beijing Municipal Science and Technology Commission and Zhongguancun Science Park Administrative Committee (No. 20251090054). JH acknowledges support from the Natural Science Foundation of Jiangsu Province (No. BK20250404), the Youth Science and Technology Talent Support Project of Jiangsu Province (No. JSTJ-2025-600).

Declarations

Competing interests

The authors declare no competing interests.

Data Availability

All data supporting this study will be made available upon publication.

Code Availability

The code supporting this study will be made available upon publication.

A Benchmark Task Suite

QCTRL-Bench comprises sixteen quantum control tasks, each probing a distinct aspect of control synthesis. The tasks are presented below in their canonical ordering, with the underlying physics and control objective specified for each.

A.1 Task I: Qubit Ground-State Transfer

Counter-diabatic (CD) driving, also known as shortcuts to adiabaticity, enables high-fidelity quantum state transfer through an auxiliary control field that cancels diabatic transitions [41, 42]. This task extends CD driving to time-dependent parameters using higher-order polynomial ramps to ensure smoothness.

Hamiltonian.

The system Hamiltonian is defined in terms of a time-dependent tunneling amplitude $\Delta(t)$ and a longitudinal field $\nu(t)$:

$$H(t) = \Delta(t)\sigma^x + \nu(t)\sigma^z - g(t)\sigma^y, \quad (7)$$

where $g(t)$ is the CD control field to be optimized. The system parameters evolve according to

$$\Delta(t) = \Delta_0 \left[1 + \left(\frac{t}{T} \right)^3 \right], \quad \nu(t) = h_0 + (h_f - h_0) S\left(\frac{t}{T}\right), \quad (8)$$

where $S(\tau) = 10\tau^3 - 15\tau^4 + 6\tau^5$ (with $\tau = t/T$) is the quintic smoothstep function.

Exact solution.

The CD field that ensures perfect adiabatic following is given by

$$g_{\text{exact}}(t) = \frac{\Delta(t)\dot{\nu}(t) - \nu(t)\dot{\Delta}(t)}{2(\Delta(t)^2 + \nu(t)^2)}, \quad (9)$$

with $\dot{\Delta}(t) = 3\Delta_0 t^2/T^3$ and $\dot{\nu}(t) = (h_f - h_0)(30/T)\tau^2(1 - \tau)^2$ (where $\tau = t/T$).

Calibration noise.

To model hardware miscalibration, multiplicative scaling is applied to all Hamiltonian parameters,

$$\Delta_{0,\text{noisy}} = \Delta_0(1 + \delta), \quad h_{0,\text{noisy}} = h_0(1 + \delta), \quad h_{f,\text{noisy}} = h_f(1 + \delta), \quad (10)$$

and the resulting physical fidelity is reported at the representative error level $\delta = \pm 0.02$. Because global parameter scaling alters the required cancellation geometry relative to the fixed control field $g(t)$, this perturbation provides a stringent robustness test of the protocol.

A.2 Task II: Dicke State Preparation

Dicke states are symmetric multi-qubit entangled states with fixed excitation number [43]. The Dicke state $|D_{N_q}^{(k)}\rangle$ is the equal superposition of all N_q -qubit computational basis states of Hamming weight exactly k :

$$|D_{N_q}^{(k)}\rangle = \binom{N_q}{k}^{-1/2} \sum_{|\mathbf{x}|=k} |\mathbf{x}\rangle, \quad (11)$$

where the sum runs over all N_q -bit strings \mathbf{x} of Hamming weight k .

To make the underlying symmetry manifest and to reduce the effective dimension, we replace the full N_q -qubit computational basis with the symmetric collective-spin basis. The collective spin operators are defined as

$$J_\mu = \frac{1}{2} \sum_{i=1}^{N_q} \sigma_\mu^{(i)}, \quad \mu \in \{x, y, z\}, \quad (12)$$

where $\sigma_\mu^{(i)}$ is the Pauli- μ operator acting on qubit i , together with the total-spin operator $J^2 = J_x^2 + J_y^2 + J_z^2$. The fully symmetric subspace carries total spin $j = N_q/2$ and admits Dicke basis states $|j, m\rangle$ satisfying

$$J^2|j, m\rangle = j(j+1)|j, m\rangle, \quad J_z|j, m\rangle = m|j, m\rangle, \quad (13)$$

with $m \in \{-j, \dots, j\}$ [29]. Here J_z is the collective spin projection along the z axis (equivalently, the sum of the individual z components), and m is related to the excitation number k by $m = k - N_q/2$. The symmetric weight- k superposition $|D_{N_q}^{(k)}\rangle$ thus coincides with $|j, m\rangle$, and the all-zero state satisfies $|0 \cdots 0\rangle \equiv |j, -j\rangle$.

We consider a collective-spin Hamiltonian with two phase controls,

$$H(x_1, x_2) = \omega [\cos(x_1)J_x + \cos(x_2)J_y] + \beta J_z^2, \quad (14)$$

where J_x, J_y, J_z act on the symmetric subspace. The controls are piecewise-constant phase sequences $x_1[t], x_2[t] \in [-\pi, \pi]$ discretized into N_t time slices of duration $\Delta t = T/N_t$. The resulting evolution is

$$U(T) = \prod_{i=1}^{N_t} \exp(-iH(x_1^i, x_2^i) \Delta t), \quad (15)$$

$$|\psi(T)\rangle = U(T)|\psi(0)\rangle,$$

and solutions are evaluated by the state fidelity $F = |\langle D_{N_q}^{(k)} | \psi(T) \rangle|^2$.

GRAPE optimization.

As a classical baseline, the piecewise-constant phases are optimized via a GRAPE-style discretization: the loss $\mathcal{J} = 1 - F$ is minimized over the $2N_t$ decision variables

$\{x_1^i, x_2^i\}_{i=1}^{N_t}$ using a quasi-Newton method such as L-BFGS-B [9]. Robustness to calibration errors is additionally probed by evaluating the resulting pulse under multiplicative miscalibration of (ω, β) .

Calibration noise.

Hardware miscalibration is modeled by multiplicative scaling of the Hamiltonian parameters,

$$\omega_{\text{noisy}} = \omega(1 + \delta), \quad \beta_{\text{noisy}} = \beta(1 + \delta), \quad (16)$$

and the resulting physical fidelity is reported at the representative error level $\delta = \pm 0.02$. This stress-tests whether proposed pulses remain effective when both the transverse driving and the interaction strength drift together.

A.3 Task III: Avoided-Crossing State Transfer

The Landau-Zener model [44, 45] considers a two-level system (qubit) governed by the time-dependent Hamiltonian

$$H(t) = \Delta \sigma_x + \nu(t) \sigma_z, \quad (17)$$

where σ_x and σ_z are Pauli matrices, Δ is a constant transverse tunnel coupling, and $\nu(t)$ is the time-dependent longitudinal detuning. The instantaneous eigenenergies are $E_{\pm}(\nu) = \pm\sqrt{\Delta^2 + \nu^2}$, with corresponding excited-state eigenvector

$$|\phi(\nu)\rangle = \cos(\theta/2)|0\rangle + \sin(\theta/2)|1\rangle, \quad \tan \theta = \Delta/\nu. \quad (18)$$

In the present numerical studies we fix $\Delta = 1.2$ and a total sweep range $\nu(t) \in [-\nu_{\text{limit}}, +\nu_{\text{limit}}]$ with $\nu_{\text{limit}} = 3$. The objective is to obtain from the LLM an optimal control protocol $\nu(t)$ that drives the system from the initial state $|\psi_0\rangle = |\phi(-\nu_0)\rangle$ to the target state $|\psi_*\rangle = |\phi(+\nu_0)\rangle$ within a fixed duration $T = \pi/2$, with $\nu_0 = 3$.

The control field $\nu(t)$ is discretized into $N_t = 20$ piecewise-constant time slices of duration $\delta t = T/N_t$. The total unitary evolution operator is approximated by the product of discrete propagators,

$$U(T) = \prod_{k=1}^{N_t} \exp[-i(\Delta \sigma_x + \nu_k \sigma_z) \delta t], \quad (19)$$

where ν_k is the constant amplitude on the k -th interval. Under VF-QCTRL, the LLM emits a continuous function $f(t)$, which is sampled at the slice midpoints $t_k = (k + \frac{1}{2}) \delta t$ to obtain $\nu_k = f(t_k)$. Performance of the resulting sequence $\{\nu_k\}$ is quantified by the state fidelity

$$\mathcal{F} = |\langle \psi_* | U(T) | \psi_0 \rangle|^2. \quad (20)$$

If any ν_k supplied by the LLM falls outside $[-\nu_{\text{limit}}, +\nu_{\text{limit}}]$, the evaluator returns $\mathcal{F} = 0$ as a penalty; this rule is disclosed to the LLM in the prompt.

The task evaluates the ability of the LLM to maximize the final-state fidelity \mathcal{F} . We benchmark a range of LLMs and prompt strategies against classical numerical

methods including GRAPE (Gradient Ascent Pulse Engineering) and a gradient-free CRAB (Chopped Random Basis) optimizer [11]. To assess robustness, evaluations are conducted across several noise levels: a noise level of $M\%$ is implemented by scaling the transverse coupling Δ by a factor of $(1 + M\%)$. The actual value of Δ is withheld from the LLM during optimization, so that the model must discover effective control sequences through a purely black-box iterative feedback loop.

A.4 Task IV: Phase-Modulated Qubit Rotation

Unitary synthesis generalizes state preparation: rather than mapping a single initial state to a single target, the goal is to implement an entire unitary transformation $U_{\text{target}} \in \text{SU}(2)$ over a fixed duration T using phase-only control.

We consider a resonantly driven two-level system in the rotating frame (within the rotating-wave approximation) with a fixed drive amplitude and phase-only control [1]. The qubit evolves under the time-dependent Hamiltonian

$$H(t) = \frac{\Omega}{2} [\cos \alpha(t) \sigma_x + \sin \alpha(t) \sigma_y], \quad (21)$$

where σ_x, σ_y are Pauli operators, Ω is the (constant) Rabi frequency—the angular rate of coherent rotations under resonant driving—and $\alpha(t)$ is the control phase, which selects the instantaneous rotation axis within the equatorial (x - y) plane of the Bloch sphere ($\alpha = 0$ corresponds to an x -axis drive and $\alpha = \pi/2$ to a y -axis drive). The closed-system propagator satisfies the Schrödinger equation

$$\dot{U}(t) = -iH(t)U(t), \quad U(0) = \mathbb{I}. \quad (22)$$

Following a GRAPE-style discretization, the control is parameterized as N_t piecewise-constant segments over the fixed duration T : with $\Delta t = T/N_t$ and $\alpha(t) = \alpha_k$ for $t \in [k\Delta t, (k+1)\Delta t)$, the final unitary is

$$U(T) = \prod_{k=0}^{N_t-1} \exp(-iH(\alpha_k)\Delta t), \quad \alpha_k \in [-\pi, \pi]. \quad (23)$$

Solutions are evaluated using the trace-overlap gate fidelity $F_{\text{gate}}(U_{\text{target}}, U(T))$ of Eq. (6) with $d = 2$, which is invariant under an overall (global) phase of $U(T)$. Because $H(t)$ generates only equatorial rotations, the target gate is generically misaligned with the instantaneous control axis; universal single-qubit control therefore requires time-varying phase patterns that compose multiple non-commuting rotations. In particular, composite phase modulation can synthesize effective z -axis rotations such as $U_z(\pi) = \exp(-i\sigma_z\pi/2)$ despite the absence of a direct σ_z control term. This task tests whether the LLM can reason about universal control from constrained Hamiltonians and produce phase sequences that realize a full target unitary rather than a single state transfer.

GRAPE optimization.

As a classical baseline, the phase sequence $\{\alpha_k\}_{k=0}^{N_t-1}$ is optimized under the same discretization by minimizing $\mathcal{J} = 1 - F_{\text{gate}}$ with GRAPE-style gradients (e.g., using a quasi-Newton method such as L-BFGS-B).

Calibration noise.

Drive miscalibration is modeled by multiplicative scaling of the Rabi coefficient,

$$\Omega_{\text{noisy}} = \Omega(1 + \delta), \quad (24)$$

and the resulting physical performance is reported at the representative error level $\delta = \pm 0.02$.

A.5 Task V: Two-Qubit State Transfer

This task targets the transfer from an initial product state $|\psi_0\rangle = |00\rangle$ to the target $|\psi_{\text{targ}}\rangle = |11\rangle$ through a controllable inter-qubit coupling. The system evolves under an Ising-type Hamiltonian with fixed random drift coefficients and a single interaction control:

$$H(t) = \sum_{i=1}^2 \left(\alpha_i \sigma_x^{(i)} + \beta_i \sigma_z^{(i)} \right) + u(t) \sigma_z^{(1)} \sigma_z^{(2)}, \quad (25)$$

where $\alpha_i, \beta_i \in [0, 1]$ are fixed random drift coefficients drawn from a predetermined seed (ensuring reproducibility across evaluations), and $u(t)$ is a piecewise-constant control field that modulates the Ising interaction strength [9]. The state-transfer fidelity is $F = |\langle \psi_{\text{targ}} | \psi(T) \rangle|^2$.

The control is discretized into $N_t = 25$ time slices with total evolution time $T = 18$. This task probes the ability of the LLM to reason about entanglement generation through controllable interactions and to navigate optimization landscapes induced by random drift Hamiltonians that break rotational symmetries.

A.6 Task VI: Controlled-Phase Gate Synthesis

The controlled-phase (CPHASE) gate is a fundamental two-qubit entangling operation that applies a phase ϕ to the $|11\rangle$ state [9]:

$$U_{\text{CPHASE}}(\phi) = \text{diag}(1, 1, 1, e^{i\phi}), \quad (26)$$

where $\phi = \pi$ yields the controlled- Z gate. The system Hamiltonian includes a calibration-induced drift term and seven control channels:

$$H(t) = (\kappa - 1) \sigma_x^{(1)} \sigma_x^{(2)} + \sum_{i=1}^2 \vec{u}_i(t) \cdot \vec{\sigma}^{(i)} + u_{\text{db}}(t) \sum_{\mu \in \{x,y,z\}} \sigma_\mu^{(1)} \sigma_\mu^{(2)}, \quad (27)$$

where $\vec{u}_i(t) = (u_{ix}, u_{iy}, u_{iz})$ and $\vec{\sigma} = (\sigma_x, \sigma_y, \sigma_z)$. Here κ is a calibration parameter (nominally $\kappa = 1$, so that the drift term vanishes in the noiseless case), and $u_{\text{db}}(t)$

is a single interaction channel. The gate fidelity is evaluated using the trace-overlap measure $F_{\text{gate}}(U_{\text{target}}, U(T))$ of Eq. (6) with $d = 4$.

The control is discretized into $N_t = 25$ time slices with total evolution time $T = 2\pi$. This task probes the ability of the LLM to synthesize high-fidelity two-qubit gates through coordinated multi-channel control.

A.7 Task VII: Damped-Qubit Hadamard Gate

Open quantum systems require control design in the presence of dissipation and decoherence. This task targets implementation of the Hadamard gate $H = \frac{1}{\sqrt{2}}(\sigma_x + \sigma_z)$ on a single qubit subject to amplitude damping, described by the Lindblad master equation [46, 47]

$$\frac{d\rho}{dt} = \mathcal{L}[\rho] = -i[H(t), \rho] + \gamma (\sigma_- \rho \sigma_+ - \frac{1}{2} \{\sigma_+ \sigma_-, \rho\}), \quad (28)$$

where the Hamiltonian is $H(t) = \frac{\omega_q}{2} \sigma_z + \frac{\Delta}{2} \sigma_x + u_z(t) \sigma_z + u_x(t) \sigma_x$ with $\omega_q = 1.1$, $\Delta = 0.15$, and damping rate $\gamma = 0.15$. The controls $u_z(t)$ and $u_x(t)$ are piecewise-constant fields discretized into $N_t = 10$ time slices with total evolution time $T = 2$.

The evolution is computed in Liouville space as a superoperator: the initial map is $E_0 = \mathcal{I} \otimes \mathcal{I}$ (the identity superoperator) and the target is $E_{\text{targ}} = H \otimes H^*$. The fidelity is measured by the trace-difference norm,

$$F = 1 - \frac{1}{2d^2} \text{Tr}[(E_{\text{targ}} - E)^\dagger (E_{\text{targ}} - E)], \quad (29)$$

where $d = 2$ is the Hilbert-space dimension. This task evaluates the ability of the LLM to reason about non-unitary dynamics, to design robust controls that compensate for dissipation, and to operate on superoperator representations of quantum channels.

A.8 Task VIII: Two-Qubit Fourier Gate Synthesis

We synthesize a two-qubit Quantum Fourier Transform (QFT) gate [48] using an optimized pulse parameterization. The physical system consists of two qubits coupled via an isotropic Heisenberg interaction with fixed coupling strength $J = 0.618$, described by the drift Hamiltonian

$$H_{\text{drift}} = J (\sigma_x^{(1)} \sigma_x^{(2)} + \sigma_y^{(1)} \sigma_y^{(2)} + \sigma_z^{(1)} \sigma_z^{(2)}). \quad (30)$$

The control Hamiltonian provides independent driving of each qubit along the x and y axes, so that the total time-dependent Hamiltonian is

$$H(t) = H_{\text{drift}} + \sum_{q=1}^2 \left[u_{x,q}(t) \sigma_x^{(q)} + u_{y,q}(t) \sigma_y^{(q)} \right], \quad (31)$$

where the controls $u_{k,q}(t)$ are continuous functions parameterized by a truncated Fourier series. The objective is to maximize the gate fidelity $F_{\text{gate}}(U_{\text{target}}, U(T))$ of Eq. (6) with $d = 4$, with respect to the canonical two-qubit QFT unitary.

A.9 Task IX: Dissipative Lambda Transfer

Population transfer in a three-level Λ -system is modeled by a non-Hermitian effective Hamiltonian that accounts for the lossy intermediate state $|2\rangle$ with decay rate $\gamma = 0.4$. In the rotating frame, with complex pump (Ω_P) and Stokes (Ω_S) fields, the Hamiltonian reads

$$H_{\text{eff}}(t) = \begin{pmatrix} \Delta_P & -\frac{1}{2}\Omega_P(t) & 0 \\ -\frac{1}{2}\Omega_P^*(t) & -i\gamma & -\frac{1}{2}\Omega_S(t) \\ 0 & -\frac{1}{2}\Omega_S^*(t) & \Delta_S \end{pmatrix}, \quad (32)$$

where Δ_P and Δ_S denote the detunings of the pump and Stokes lasers, respectively. The objective is to transfer population efficiently from the initial state $|1\rangle$ to the target state $|3\rangle$, typically by invoking the Stimulated Raman Adiabatic Passage (STIRAP) mechanism [49] so as to avoid populating the lossy intermediate state $|2\rangle$.

A.10 Task X: Driftless Single-Qubit Gate

This task evaluates full controllability on the single-qubit Bloch sphere [8]. In contrast to settings with restricted interactions, the agent here has control over all three Pauli generators, with Hamiltonian

$$H(t) = u_x(t)\sigma_x + u_y(t)\sigma_y + u_z(t)\sigma_z. \quad (33)$$

The control inputs u_x, u_y, u_z are piecewise-constant fields. For each problem instance, a random target unitary $U_{\text{target}} \in \text{SU}(2)$ is generated via Euler angles,

$$U_{\text{target}} = R_z(\phi) R_x(\theta) = e^{-i\phi\sigma_z/2} e^{-i\theta\sigma_x/2}. \quad (34)$$

The objective is to synthesize U_{target} with high fidelity, thereby testing the ability to coordinate simultaneous rotations about non-commuting axes.

A.11 Task XI: Coupled-Oscillator Symplectic Transform

This task involves the control of two coupled harmonic oscillators in the continuous-variable regime [50], described by the evolution of an element $S(t)$ in the symplectic group $\text{Sp}(4, \mathbb{R})$. The dynamics are governed by

$$\dot{S}(t) = \Omega H_{\text{total}}(t) S(t), \quad (35)$$

where Ω is the symplectic form and the generator is $G(t) = \Omega [A_0 + u(t) A_c]$. With phase-space vector $x = (q_1, p_1, q_2, p_2)^T$, the quadratic Hamiltonian is $H = \frac{1}{2}x^T A x$,

and the drift and control matrices are

$$A_0 = \begin{pmatrix} \omega_1 & 0 & g_1 & 0 \\ 0 & \omega_1 & 0 & g_1 \\ g_1 & 0 & \omega_2 & 0 \\ 0 & g_1 & 0 & \omega_2 \end{pmatrix}, \quad A_c = \begin{pmatrix} 1 & 0 & 0 & 0 \\ 0 & 1 & 0 & 0 \\ 0 & 0 & 0 & 0 \\ 0 & 0 & 0 & 0 \end{pmatrix}, \quad (36)$$

with $\omega_1 = \omega_2 = 1.414$ and $g_1 = 0.5$. The symplectic form is

$$\Omega = \begin{pmatrix} 0 & I_2 \\ -I_2 & 0 \end{pmatrix}. \quad (37)$$

The goal is to steer the system from the identity I_4 to a target symplectic rotation $S_{\text{target}} = \exp(\Omega)$.

A.12 Task XII: Toffoli Gate Synthesis

The Toffoli (CCNOT) gate [51] is optimized on a linear chain of three qubits. The system comprises a constant drift term describing the qubit frequencies and a set of controllable interaction terms,

$$H(t) = H_0 + \sum_k c_k(t) H_k^{\text{ctrl}}, \quad (38)$$

with drift Hamiltonian $H_0 = 2\pi \sum_{j=1}^3 \sigma_z^{(j)}$. The control set $\{H_k^{\text{ctrl}}\}$ comprises 18 operators covering both single-qubit rotations and pairwise interactions,

$$\{H_k^{\text{ctrl}}\} = \{\sigma_\alpha^{(j)}\} \cup \{\sigma_\alpha^{(i)} \sigma_\alpha^{(j)}\}, \quad \alpha \in \{x, y, z\}, \quad (39)$$

where the pairwise terms act on the connected neighbors (1, 2) and (2, 3), with additional non-adjacent pairs included subject to connectivity. The objective is to realize the three-qubit Toffoli gate U_{Toffoli} at maximal process fidelity in the eight-dimensional Hilbert space.

A.13 Task XIII: Transmon Logical X Gate

This task optimizes a logical Pauli- X gate on a multilevel transmon qubit [5, 52] in the charge basis. With basis states $\{|j\rangle\}_{j=-N_c}^{N_c}$, the drift Hamiltonian is

$$H_0 = 4E_C \sum_{j=-N_c}^{N_c} (j - n_g)^2 |j\rangle\langle j| - \frac{E_J}{2} \sum_{j=-N_c}^{N_c-1} (|j+1\rangle\langle j| + |j\rangle\langle j+1|). \quad (40)$$

Control enters through the charge operator

$$q = \sum_{j=-N_c}^{N_c} (-2j) |j\rangle\langle j|, \quad (41)$$

so that the full Hamiltonian reads

$$H(t) = H_0 + V(t) q, \quad (42)$$

with a single real control channel $V(t)$. The benchmark physical parameters are

$$N_c = 8, \quad E_C = 0.386 \text{ GHz}, \quad E_J = 15.44 \text{ GHz}, \quad n_g = 0, \quad (43)$$

yielding a Hilbert-space dimension $2N_c + 1 = 17$. The total gate time is $T = 10.0$ ns, and the control is discretized into $N_t = 50$ piecewise-constant time slices.

The logical qubit is defined by the two lowest-energy eigenstates of H_0 , denoted $|0_L\rangle$ and $|1_L\rangle$, and the target operation is a logical Pauli- X on this subspace. Given the simulated unitary $U(T)$, the induced logical 2×2 block is

$$U_{\text{log}} = \begin{pmatrix} \langle 0_L | U(T) | 0_L \rangle & \langle 0_L | U(T) | 1_L \rangle \\ \langle 1_L | U(T) | 0_L \rangle & \langle 1_L | U(T) | 1_L \rangle \end{pmatrix}, \quad (44)$$

and the solution is evaluated by the logical gate fidelity $F_{\text{gate}}(X, U_{\text{log}})$ of Eq. (6) with $d = 2$, where $X = \begin{pmatrix} 0 & 1 \\ 1 & 0 \end{pmatrix}$. The optimization objective is therefore the minimization of $\mathcal{J} = 1 - F_{\text{gate}}$.

A.14 Task XIV: Leakage-Aware Transmon Excitation

This task optimizes a leakage-suppressed π pulse [53] for a three-level transmon model with computational states $|0\rangle, |1\rangle$ and leakage state $|2\rangle$. The Hamiltonian is

$$H(t) = \delta(t) |1\rangle\langle 1| + (2\delta(t) - \alpha) |2\rangle\langle 2| + \frac{\Omega_x(t)}{2} M_x + \frac{\Omega_y(t)}{2} M_y, \quad (45)$$

with

$$M_x = |0\rangle\langle 1| + \lambda |1\rangle\langle 2| + \text{h.c.}, \quad M_y = -i |0\rangle\langle 1| - i\lambda |1\rangle\langle 2| + \text{h.c.} \quad (46)$$

Here $\Omega_x(t)$ is the in-phase drive, $\Omega_y(t)$ is the quadrature DRAG correction, and $\delta(t)$ is a detuning-compensation channel. The benchmark parameters are

$$\alpha = 0.3 \text{ GHz}, \quad \lambda = \sqrt{2} \approx 1.414214, \quad T = 60.0 \text{ ns}, \quad N_t = 50, \quad (47)$$

with piecewise-constant controls over N_t equal time slices.

The system starts in the ground state $|\psi(0)\rangle = |0\rangle$, and the target is a π -pulse into $|\psi_{\text{target}}\rangle = |1\rangle$. For a piecewise-constant control sequence, the final state is

$$|\psi(T)\rangle = \prod_{k=1}^{N_t} \exp(-iH_k \Delta t) |0\rangle. \quad (48)$$

The pulse is evaluated by the target-state fidelity $F = |\langle 1 | \psi(T) \rangle|^2$, and the controls are optimized by minimizing the infidelity $\mathcal{J} = 1 - F$.

Calibration noise.

Hardware miscalibration is modeled by multiplicative scaling of the anharmonicity,

$$\alpha_{\text{noisy}} = \alpha(1 + \delta_\kappa), \quad (49)$$

and the resulting state fidelity is reported at the representative error level $\delta_\kappa = \pm 0.02$. This stress-tests whether the proposed pulses remain effective when the transmon's frequency structure drifts.

A.15 Task XV: NMR Coherence Transfer

This task considers coherence transfer in a weakly coupled heteronuclear two-spin NMR system. Let

$$S_1^\mu = \frac{\sigma_\mu}{2} \otimes \mathbb{I}_2, \quad S_2^\mu = \mathbb{I}_2 \otimes \frac{\sigma_\mu}{2}, \quad \mu \in \{x, y, z\}, \quad (50)$$

where the first tensor factor acts on spin 1 and the second on spin 2. The time-dependent Hamiltonian is

$$H(t) = 2\pi J S_1^z S_2^z + u_1^x(t) S_1^x + u_1^y(t) S_1^y + u_2^x(t) S_2^x + u_2^y(t) S_2^y, \quad (51)$$

where J is the scalar coupling constant and $u_1^x, u_1^y, u_2^x, u_2^y$ are the four RF control channels. The benchmark parameters are

$$J = 100 \text{ Hz}, \quad T = 15.0 \text{ ms}, \quad N_t = 60, \quad (52)$$

so that the controls are discretized into N_t piecewise-constant time slices of duration $\Delta t = T/N_t = 0.25$ ms.

The initial and target operators are $\rho(0) = S_2^x$ and $\rho_{\text{target}} = S_1^x$, respectively. For a piecewise-constant control sequence, the evolution is

$$\rho(T) = U(T) \rho(0) U^\dagger(T), \quad U(T) = \prod_{k=1}^{N_t} \exp(-iH_k \Delta t), \quad (53)$$

where H_k denotes the Hamiltonian on the k -th time slice. The optimization objective is to maximize the polarization-transfer efficiency

$$F_{\text{transfer}} = \text{Tr}(S_1^x \rho(T)), \quad (54)$$

equivalently to minimize the infidelity $\mathcal{J} = 1 - F_{\text{transfer}}$. With $S_1^x = \sigma_x/2 \otimes \mathbb{I}_2$ normalized so that $\text{Tr}((S_1^x)^2) = 1$, F_{transfer} coincides with the state-overlap fidelity of Eq. (6) whenever $\rho(T)$ is a pure state aligned with the target operator; it takes values in $[-1, +1]$ under unitary evolution and attains $F_{\text{transfer}} = 1$ for perfect transfer.

Analytical solution.

The time-optimal transfer is achieved by the INEPT (Insensitive Nuclei Enhanced by Polarization Transfer) sequence [54], which consists of carefully timed $\pi/2$ pulses interleaved with free evolution under the J -coupling. In the product-operator formalism the theoretical pathway is

$$S_2^x \xrightarrow{\tau=1/(4J)} 2 S_1^z S_2^y \xrightarrow{(\pi/2)S_1^x} 2 S_1^y S_2^y \xrightarrow{\tau=1/(4J)} S_1^x, \quad (55)$$

where $\tau = 1/(4J) = 2.5$ ms for $J = 100$ Hz. Under ideal conditions this analytical solution attains $F_{\text{transfer}} = 1$ (perfect transfer).

Calibration noise.

Hardware miscalibration is modeled by multiplicative scaling of the coupling constant,

$$J_{\text{noisy}} = J(1 + \delta), \quad (56)$$

and the resulting transfer efficiency is reported at the representative error level $\delta = \pm 0.02$. This stress-tests whether the proposed pulse sequences remain effective when the J -coupling strength deviates from its nominal value.

A.16 Task XVI: Polynomial-Noise Qubit Refocusing

This task inverts the usual gate-synthesis objective: the control is required to act trivially—the qubit should return to its initial state—despite a known, time-dependent dephasing term that would otherwise rotate it. The LLM must therefore design a control pulse whose effect exactly cancels the noise-induced dephasing over the evolution, a dynamical-decoupling problem.

Hamiltonian.

A single qubit evolves under

$$H(t) = \frac{\beta(t)}{2} \sigma_z + \frac{\Omega(t)}{2} \sigma_x, \quad (57)$$

where $\beta(t)$ is a deterministic σ_z disturbance (a time-varying detuning) and $\Omega(t)$ is the σ_x control to be optimized. The disturbance has polynomial structure,

$$\beta(t) = \beta_0 + \beta_1 t + \beta_2 t^2, \quad (58)$$

with default parameters $(\beta_0, \beta_1, \beta_2) = (0.5, 2.0, 20.0)$. The constant, linear, and quadratic components jointly probe whether the LLM can refocus non-stationary noise rather than only DC dephasing.

Control and evolution.

The control $\Omega(t)$ is discretized into $N_t = 100$ piecewise-constant segments over total evolution time $T = 1$. Slice k samples β at its midpoint $t_k = (k - \frac{1}{2}) \Delta t$, with $\Delta t = T/N_t$, giving

$$U(T) = \prod_{k=1}^{N_t} \exp \left[-i H(\Omega_k, \beta(t_k)) \Delta t \right]. \quad (59)$$

Objective.

The target operation is the identity, $U_{\text{target}} = \mathbb{I}$. Performance is measured by the gate-overlap fidelity $F_{\text{gate}}(\mathbb{I}, U(T))$ of Eq. (6) with $d = 2$, which rewards any $\Omega(t)$ whose evolution, combined with the unavoidable σ_z drive, returns the qubit to the identity up to a global phase. Standard analytical baselines in this regime are the Carr–Purcell and XY pulse trains [55, 56], which apply σ_x π -pulses at times chosen so as to refocus the accumulated dephasing into a closed loop on the Bloch sphere.

Calibration noise.

Hardware miscalibration is modeled by a multiplicative scaling applied jointly to all noise parameters,

$$\beta_{k,\text{noisy}} = \beta_k(1 + \delta), \quad k \in \{0, 1, 2\}, \quad (60)$$

with $\delta = \pm 0.02$. The LLM is provided with the nominal coefficients, whereas the evaluator uses the perturbed values; this stress-tests whether the proposed pulses remain effective when the dephasing profile drifts simultaneously in amplitude and slope.

B Efficiency and per-model breakdowns

B.1 Query efficiency vs. the classical baseline

Beyond final fidelity, the cost to reach a target fidelity matters. We measure cost as the number of queries needed to first cross $F = 0.999$. For the classical baseline this is the SPSA iteration index, capped at 5×10^4 . For VF-QCTRL it is outer-loop iterations number 10^3 (the per-round inner coefficient-optimizer budget).

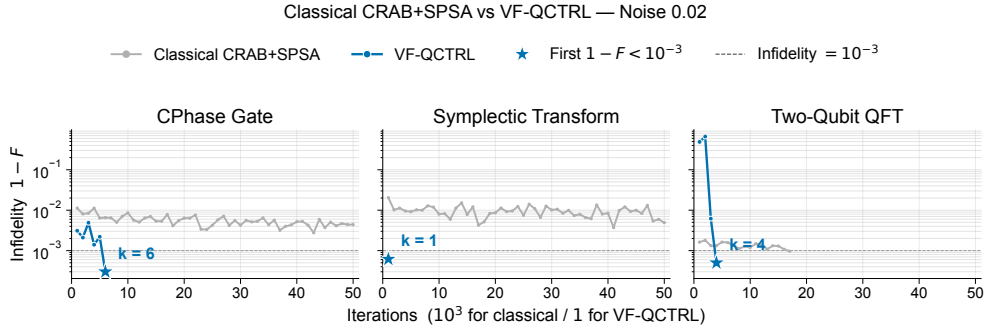


Fig. 6: Convergence trajectories at $\sigma = 0.02$ for three representative tasks. Infidelity $1 - F$ (log scale) versus a shared iteration index for the classical baseline (grey) and VF-QCTRL (blue) on (a) Controlled-Phase Gate Synthesis, (b) Coupled-Oscillator Symplectic Transform, and (c) Two-Qubit Fourier Gate Synthesis. One unit on the horizontal axis corresponds to 1000 coefficient updates (CRAB+SPSA for classical baseline; inner coefficient-optimizer updates for VF-QCTRL), placing the two methods on matched budgets. The dashed horizontal line marks the threshold $1 - F = 10^{-3}$ ($F = 0.999$); blue stars mark the first VF-QCTRL outer-loop iterations at which the threshold is crossed. The classical baseline does not cross the threshold within 50000 iterations on (a) or (b), and first crosses it at iteration 17,000 on (c).

Figure 6 shows convergence trajectories at $\sigma = 0.02$ for three representative tasks: Controlled-Phase Gate Synthesis, Coupled-Oscillator Symplectic Transform, and Two-Qubit Fourier Gate Synthesis. VF-QCTRL crosses $F = 0.999$ within at most 6 outer-loop iterations (6×10^3 iterations) on all three. The classical baseline does not cross the threshold within 5×10^4 iterations on Controlled-Phase Gate Synthesis or Coupled-Oscillator Symplectic Transform, and first crosses it only at iteration 17,000 on Two-Qubit Fourier Gate Synthesis, between $4 \times$ (Two-Qubit Fourier Gate Synthesis) and $\geq 50 \times$ (Coupled-Oscillator Symplectic Transform) later in iteration number than VF-QCTRL. The contrast reflects the dimensional-reduction mechanism of form proposal: once the LLM has committed to a compact analytic ansatz, the inner coefficient optimizer refines a handful of coefficients rather than tens of pulse amplitudes per channel.

B.2 Token efficiency vs. pure-LLM baselines

VF-QCTRL token cost is comparable to or less than the pure-LLM methods across all evaluated LLMs and both noise levels. Per LLM, VF-QCTRL ranges over roughly 0.4–1.05 million tokens; Hint LLM and Simple LLM range over 0.4–1.45 million. The asymmetry is largest for Qwen 3.5 Plus, where VF-QCTRL uses ~ 0.5 – 0.85 M tokens versus ~ 1.4 M for the two pure-LLM methods.

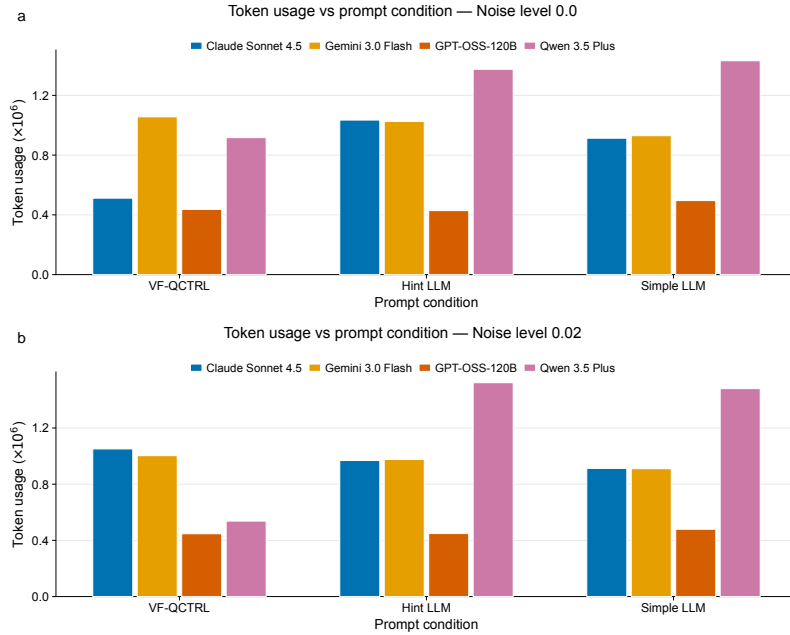


Fig. 7: Average total token consumption by method, model, and noise level. Total tokens for the best run, averaged over the sixteen tasks. Methods on the x-axis are VF-QCTRL, Hint LLM, and Simple LLM, coloured by LLM (Claude Sonnet 4.5, Gemini 3.0 Flash, GPT-OSS-120B, Qwen 3.5 Plus). **(a)** $\sigma = 0$. **(b)** $\sigma = 0.02$. For every LLM, VF-QCTRL consumes comparable or fewer tokens than the two pure-LLM methods.

B.3 Per-model fidelity at $\sigma = 0$

Under VF-QCTRL the four-model mean-fidelity spread is small compared to the pure-LLM methods. The pattern matches the $\sigma = 0.02$ result in main-text Figure 3: once the LLM has proposed the right functional form, the remaining coefficient optimization largely absorbs the model-capability gap.

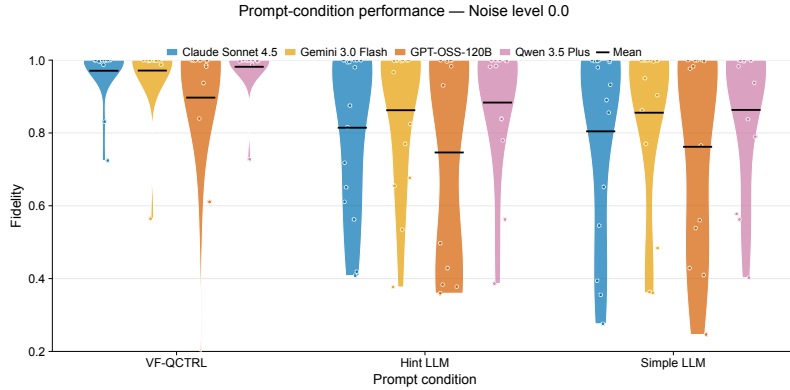


Fig. 8: Per-task best-fidelity distribution at $\sigma = 0$. Violin plots of the per-task best fidelity over the sixteen QCTRL-Bench tasks, grouped by method (VF-QCTRL, Hint LLM, Simple LLM) and coloured by LLM (Claude Sonnet 4.5, Gemini 3.0 Flash, GPT-OSS-120B, Qwen 3.5 Plus); the horizontal black tick on each violin marks the per-cell mean.

C Iteration-prompt templates: rendered examples

This appendix shows the actual prompts the proposal agent receives at iteration $k \geq 2$, with every template variable substituted by its rendered value for the Dicke-state task (Appendix A, Task II). The intent is to make concrete the three-block structure described in Methods, Section 3.1: a task specification (Hamiltonian, controls, target, constraints, output schema), a physics-guidance block (the `hint_prompt`), and a rolling feedback memory (the `previous_repetitions`, the best-so-far metric, the reflection-agent feedback bullets, and a trailing instruction). The two figures correspond to the two methods that consume the template:

- Figure 9 renders `iteration_n.md`, the *numeric-controls* template used by the pure-LLM baselines (Simple LLM, Hint LLM). The model is asked to emit per-time-slice amplitude arrays `x1[t]` and `x2[t]` of length 50, together with a free-form reflection-agent note carried forward as feedback.
- Figure 10 renders `iteration_n_function_class.md`, the *function-class* template used by VF-QCTRL. The system block now declares a parameterized symbolic grammar, the previous-repetitions memory stores analytic expressions instead of numeric arrays, and the trailing instruction steers the proposal agent to make the smallest structural change that improves the metric.

In both figures the colored pill above each bubble names the template variable; the bubble below shows its substituted content. Section headers inside the bubbles (PHYSICS, CONTROLS, GOAL, ...) are highlighted in blue. Gray lines marked with “...” or trailing “# ...” annotations are editorial elisions added for the figure only; they are *not* part of the prompt text seen by the model. The full unelided templates ship with the open-source repository.

One directive in the `hint_prompt` block of both figures warrants a brief note. The instruction “**DO NOT show reasoning!**” asks the model not to inline its chain-of-thought into the response body. Without it, some models inline long reasoning traces alongside the pulse output, which grows the context across iterations and crowds out the rolling feedback memory once the number of returned parameters is large; this is a practical context-window safeguard, not a constraint on the underlying reasoning step. On reasoning-capable models the chain-of-thought is still emitted through the provider’s dedicated reasoning channel where one exists, and is not parsed into the evaluation pipeline, so the directive controls placement only and does not affect the reported fidelity.

C.1 Full text of the Hint LLM physics-guidance prompt

The block below reproduces verbatim the content of the `hint_prompt` template used by the Hint LLM baseline (Methods, Section 3.3). It is appended to every iteration prompt the Hint LLM receives, between the task specification and the rolling feedback memory. The Simple LLM baseline replaces this entire block with the single line “**Think!!**” and is therefore not reproduced separately.

THINK!!

Realizing that the coefficient in this simulation might be affected by experimental condition. Identify the system, available controls, constraints, and objective, and assess symmetry, controllability, and whether the dynamics are closed or open.

Actively survey both analytic and numerical paradigms: adiabatic and nonadiabatic control (STA, counterdiabatic driving, holonomic/geometric control), average-Hamiltonian/Magnus/Floquet engineering, invariant-based and time-optimal/bang-bang control, gradient based control (GRAPE, Krotov, GOAT, L-BFGS), gradient free optimization (CRAB, annealing, evolutionary algorithm, bayesian optimization), as well as robust control, measurement feedback, and learning-assisted methods.

Do not treat this list as exhaustive: prioritize achieving the best results by inventing hybrid or novel strategies that exploit physical structure, hidden noise effects and any feedback data, then select and execute the best-performing approach consistent with the objective and constraints.

Note: Due to systematic hardware imperfections and environmental noise, the effective physical realization may deviate from the intended model. Potential sources of deviation include: Drive Strength Miscalibration, Stray Longitudinal Fields, Control Crosstalk, Pulse Overshoot/Undershoot, Phase Reference Drift, and Nonlinear Compression.

DO NOT show reasoning!

Figure 1. iteration_n.md rendered for the Dicke-state task (normal mode).

Each pill is the template variable; the bubble below shows the actual substituted content sent to the LLM at iteration $k \geq 2$. Gray text marks elisions / annotations, not real prompt content.

system_description

Prepare a Dicke state.

PHYSICS

- 3 spin-1/2 particles, symmetric subspace (dim 4)
- $H(x_1, x_2) = 5.0 * [\cos(x_1)*x + \cos(x_2)*y] + 1.2 * Jz^2$
- Initial: $|0\dots0\rangle$ Target: $|D^3_1\rangle$

CONTROLS

- 50 time slices, $T = 6.28$
- $x_1[t], x_2[t]$ in $[-\pi, \pi]$

GOAL maximize $F = |\langle 0 | \psi(T) \rangle|^2$

OUTPUT {"x1": [50 floats], "x2": [50 floats]}

METRIC neg_log10_infidelity = $-\log_{10}(1 - F)$ # 350M format rules elided (higher is better)

hint_prompt

Think!!!

DO NOT show reasoning!

previous_attempts

PREVIOUS ATTEMPTS (oldest -> newest)

```

...
12. iter=12  neg_log10_infidelity = 0.842
    x1 = [ 0.31,  0.28, ..., -0.21]
    x2 = [-0.08,  0.05, ...,  0.29]
...
18. iter=18  neg_log10_infidelity = 1.214
    x1 = [ 0.45,  0.40, ..., -0.30]
    x2 = [-0.12,  0.10, ...,  0.35]
...
23. iter=23  neg_log10_infidelity = 1.376
    x1 = [ 0.52,  0.46, ..., -0.36]
    x2 = [-0.15,  0.13, ...,  0.40]

```

iters 1-11 elided

iters 13-17 elided

iters 19-22 elided

Best reported metric so far: neg_log10_infidelity = 1.376

feedback

+0.16 over last 5 attempts.
 Peak amplitude too low -- try larger drive near $t \sim T/2$.
 Avoid identical x_1 / x_2 phase.
 ... # extra adaptive notes elided

trailing_instruction

Propose new control parameters that improve the metric.

Fig. 9: Rendered iteration prompt for the pure-LLM baselines (iteration_n.md, numeric-controls mode), Dicke-state task. Each colored pill is a template variable (system_description, hint_prompt, previous_repetitions, feedback, trailing instruction); the bubble below shows the substituted content delivered to the LLM at iteration $k \geq 2$. In this mode the model must emit $x_1[t]$ and $x_2[t]$ as length-50 numeric arrays of pulse amplitudes; the rolling feedback memory stores those arrays verbatim. Gray text (“...” lines, trailing “# ...” annotations) marks editorial elisions only.

Figure 2. `iteration_n_function_class.md` rendered for the Dicke-state task (function-class mode).

Same pill+bubble structure; same color rules. The system bubble now describes parameterized control bases, and previous attempts list expressions instead of numeric arrays.

```

system_description
Prepare a Dicke state (FUNCTION-CLASS mode).

PHYSICS
- 3 spin-1/2 particles (dim 4)
- H(x1, x2) = 5.0 * [cos(x1)*Jx + cos(x2)*Jy] + 1.2 * Jz^2
- Initial: |0...0> Target: |D^3_1>

ROLE
- Propose parameterized bases x1(t), x2(t).
- SPSA tunes every exposed parameter (budget 1000 joint iters).
- Expose ALL knobs (amp, freq, phase, center, width, ...). Do not hard-code.

GRID 50 time slices, T = 6.28
LIMITS <= 60 params / channel, >= 1 additive term / channel
... # expression-language spec elided
... # formal JSON-schema bullets elided

GOAL maximize F = |-D|psi(T)|^2

OUTPUT {"x1":{"expression":"...", "parameters":{...}}, "x2":{...}}
METRIC neg_log10_infidelity (higher is better)

hint_prompt
THINK!!
... # noise-coefficient preamble elided

Identify system, controls, constraints, symmetry, closed-vs-open dynamics.

Survey paradigms -- invent hybrids:
STA / counterdiabatic, Magnus / Floquet,
GRAPE / Krotov / GOAT / L-BFGS,
CRAB / Bayesian / evolutionary, bang-bang,
robust / measurement-feedback / learning-assisted.

Hardware may add: drive miscalibration, stray Jz fields, crosstalk,
over/undershoot, phase drift, compression.

DO NOT show reasoning!

previous_attempts
PREVIOUS ATTEMPTS (selected: best 2 + last 2) # other iterations elided by the best-2 + last-2 selection rule
...
1. iter=8 neg_log10_infidelity = 0.687
x1_expression = "a0*sin(a1*2*pi*t/T + a2)"
x2_expression = "b0*cos(b1*2*pi*t/T)"
2. iter=15 neg_log10_infidelity = 1.103
x1_expression = "a0*sin(a1*2*pi*t/T) + a2*exp(-(t - a3)**2/a4**2)"
x2_expression = "b0*cos(b1*2*pi*t/T) + b2*tanh(b3*(t/T - b4))"
3. iter=22 neg_log10_infidelity = 1.428
x1_expression = "a0*sin(a1*pi*t/T) + a2*sin(a3*pi*t/T)"
x2_expression = "b0*cos(b1*pi*t/T) + b2*cos(b3*pi*t/T)"
4. iter=23 neg_log10_infidelity = 1.512
x1_expression = "a0*sin(a1*pi*t/T) + a2*sin(a3*pi*t/T) + a4*sinc(a5*(t - a6))"
x2_expression = "b0*cos(b1*pi*t/T) + b2*cos(b3*pi*t/T)"

Best reported metric so far: neg_log10_infidelity = 1.512

feedback
Fourier-only bases plateau near 1.4. Adding a localized Gaussian or sinc
bump helped marginally -- try a true bang-bang / tanh switch near t ~ T/2
and break the x1/x2 symmetry by a phase shift of pi/4.
SPSA budget is mostly spent re-tuning amplitudes; expose more frequencies
or a Heaviside-gated polynomial segment.
... # extra review notes elided

trailing_instruction
Propose the next parameterized basis.
- Smallest helpful change to the best one.
- Don't lock into Fourier -- try Gaussian / sinc / tanh / Heaviside.
- If promising, add 1-3 terms. If stalled, switch to a fresh idea.
- Structural changes > parameter renaming.
... # other steering bullets elided

```

Fig. 10: Rendered iteration prompt for VF-QCTRL, Dicke-state task. Same structure as Figure 9, with three differences. (i) The `system_description` now declares the parameterized symbolic grammar of Section 3.1 (at most 60 free coefficients per channel, at least one additive term, allowed operations and functions); the model must return analytic expressions `x1.expression` and `x2.expression` with named parameters, which the inner SPSA optimizer then refines under a fixed budget of 10^3 joint iterations. (ii) The `previous_repetitions` memory stores the best two and the most recent two analytic ansätze together with their optimized infidelities, not numeric pulse arrays. (iii) The trailing instruction steers the proposal agent toward the smallest structural change to the best ansatz so far, favoring new basis families (Gaussian, sinc, tanh, Heaviside) over parameter renaming. Color and elision conventions match Figure 9.

D LLM Reasoning Traces for Zero-Step Coefficient-Optimizer Tasks

This appendix provides the detailed reasoning traces generated by the Qwen 3.5 Plus model under the zero-step coefficient-optimizer setting (SPSA iteration = 0) for the three analytically structured tasks discussed in Section 1.3. In this zero-step numerical optimization setting, the LLM is provided only with the mathematical system specifications (Hamiltonian, state targets, constraints, and time discretization) in the prompt and must propose both the functional form and the starting parameters without any subsequent SPSA parameter updates. The traces below are reproduced verbatim from the original logs, with irrelevant search steps or formatting operations replaced by [...] for readability.

D.1 Qubit Ground-State Transfer

System Prompt Specifications:

SYSTEM:

- Hamiltonian: $H_g(t) = [1.0 * (1 + (t/1.2)^3)]\sigma_x + [2.0 + (-2.0 - 2.0) * (10*(t/1.2)^3 - 15*(t/1.2)^4 + 6*(t/1.2)^5)]\sigma_z - g(t)\sigma_y$
- Goal: Transfer from ground state at $t=0$ to ground state at $t=T$
- Time Discretization: 40 slices over total time $T = 1.2$

Verbatim LLM Reasoning Trace:

[...]

Wait, the control $g(t)$ is part of the total Hamiltonian.

If we want to follow the ground state of $H_{\text{drift}}(t) = \Omega_x(t) \sigma^x + \Omega_z(t) \sigma^z$, we need to add a CD term.

The CD term for a spin in a magnetic field $\vec{B}_0(t)$ is

$$H_{\text{CD}} = \frac{\vec{B}_0 \times \dot{\vec{B}}_0}{|\vec{B}_0|^2} \cdot \sigma$$

Here $\vec{B}_0 = (\Omega_x, 0, \Omega_z)$.

$$\dot{\vec{B}}_0 = (\dot{\Omega}_x, 0, \dot{\Omega}_z)$$

$$\vec{B}_0 \times \dot{\vec{B}}_0 = (0, \Omega_z \dot{\Omega}_x - \Omega_x \dot{\Omega}_z, 0)$$

So the CD term is along σ^y .

$$H_{\text{CD}} = \frac{\Omega_z \dot{\Omega}_x - \Omega_x \dot{\Omega}_z}{(\Omega_x^2 + \Omega_z^2)} \sigma^y$$

Our control term is $-g(t) \sigma^y$.

$$\text{So we should set } -g(t) = \frac{\Omega_z \dot{\Omega}_x - \Omega_x \dot{\Omega}_z}{(\Omega_x^2 + \Omega_z^2)}$$

$$\text{Or } g(t) = \frac{\Omega_x \dot{\Omega}_z - \Omega_z \dot{\Omega}_x}{(\Omega_x^2 + \Omega_z^2)}$$

[...]

Let $\theta(t)$ be the angle of the field in the X-Z plane.

The instantaneous eigenstates rotate in the X-Z plane. To track the ground state, we need a rotation around Y.

The counter-diabatic driving term required to suppress transitions is roughly

$\dot{\theta}/2 \sigma_y$.
 $\tan \theta = \omega_x / \omega_z$.
 $\dot{\theta} = \frac{\omega_z \dot{\omega}_x - \omega_x \dot{\omega}_z}{\omega_x^2 + \omega_z^2}$.
 So $H_{CD} = \frac{\dot{\theta}^2}{2} \sigma_y$.
 Control term in H is $-g(t) \sigma_y$.
 So $-g = \dot{\theta}/2$ implies $g = -\dot{\theta}/2$.
 $g(t) = \frac{\omega_x \dot{\omega}_z - \omega_z \dot{\omega}_x}{2(\omega_x^2 + \omega_z^2)}$.
 [...]

So the physics is correct.
 The error must be discretization.
 Midpoint rule is 2nd order. Error $\sim dt^2 \sim 10^{-3}$.
 The CD term cancels transitions in continuous time.
 In discrete time, the "kick" from $H(t_k)$ is exact for that slice,
 but the sequence of rotations doesn't perfectly track.
 [...]

D.2 NMR Coherence Transfer

System Prompt Specifications:

SYSTEM:

- Hamiltonian: $H(t) = 2\pi J I_z S_z + u_{Ix}(t) I_x + u_{Iy}(t) I_y + u_{Sx}(t) S_x + u_{Sy}(t) S_y$
- Coupling constant: $J = 100.0$ Hz
- Initial state: $\rho(0) = S_x$
- Target state: $\rho(T) = I_x$
- Time Discretization: 60 slices over total time $T = 15.0$ ms

Verbatim LLM Reasoning Trace:

[...]

This is a standard INEPT (Insensitive Nuclei Enhanced by Polarization Transfer) type transfer or simply coherence transfer via scalar coupling. The coupling term $2\pi J I_z S_z$ generates anti-phase coherence. Evolution under $2\pi J I_z S_z$ for time τ :
 $S_x \xrightarrow{2\pi J I_z S_z \tau} S_x \cos(\pi J \tau) + 2 S_y I_z \sin(\pi J \tau)$.
 [...]

At $t = 1/(2J)$, $\pi J t = \pi/2$, $\cos=0$, $\sin=1$. State: $2 S_y I_z$.
 [...]

Change $90_x I$ to $90_{-x} I$: $2 S_z I_z \rightarrow 2 S_z I_y$.
 $2 S_z I_y \xrightarrow{J, 1/2J} I_x$.
 So:

1. Delay 5ms.
2. S: 90_x , I: 90_{-x} . (Simultaneous hard pulses)
3. Delay 5ms.

Total time 10ms + pulse widths.
 [...]

We need to preserve I_x from 10.25 to 15.0. Apply CW decoupling on S ($u_{Sx} = \text{large}$). This averages $I_z S_z$ to 0 (in the frame of S). Actually, if we lock S along x, $\langle S_z \rangle = 0$.

So $IzSz$ averages to 0. Ix is stable.
[...]
The sequence $R_x(90) - J(1/2J) - R_y(90) - J(1/2J) - R_x(90)$ is a standard decomposition for SWAP using Ising coupling.
[...]
Slice width $\Delta t = 15/60 = 0.25$ ms.
Midpoints: 0.125, 0.375, ..., 14.875.
If I define a pulse from 0.0 to 0.5 ms.
Midpoints covered: 0.125, 0.375. (2 slices).
Total duration sampled: $2 \times 0.25 = 0.5$ ms.
So if I set amplitude A , effective rotation is $A \times 0.5$ ms.
So $A \times 0.0005 = \pi/2$ implies $A = 3141.6$.
[...]
During the pulse, J -coupling is also active.
 $\omega \approx 6283$ rad/s. $2\pi J \approx 628$ rad/s. Ratio 10:1.
Error might be significant?
 0.25 ms $\times 628$ rad/s ≈ 0.157 rad $\approx 9^\circ$.
This is not negligible.
[...]

References

- [1] Glaser, S.J., Boscain, U., Calarco, T., Koch, C.P., Köckenberger, W., Kosloff, R., Kuprov, I., Luy, B., Schirmer, S., Schulte-Herbrüggen, T., Sugny, D., Wilhelm, F.K.: Training Schrödinger’s cat: quantum optimal control. *European Physical Journal D* **69**, 279 (2015) <https://doi.org/10.1140/epjd/e2015-60464-1>
- [2] Koch, C.P., Boscain, U., Calarco, T., Dirr, G., Filipp, S., Glaser, S.J., Kosloff, R., Montangero, S., Schulte-Herbrüggen, T., Sugny, D., Wilhelm, F.K.: Quantum optimal control in quantum technologies. strategic report on current status, visions and goals for research in Europe. *EPJ Quantum Technology* **9**, 19 (2022) <https://doi.org/10.1140/epjqt/s40507-022-00138-x>
- [3] Wright, K., Beck, K.M., Debnath, S., Amini, J.M., Nam, Y., Grzesiak, N., Chen, J.-S., Pienti, N.C., Chmielewski, M., Collins, C., Hudek, K.M., Mizrahi, J., Wong-Campos, J.D., Allen, S., Apisdorf, J., Solomon, P., Williams, M., Ducore, A.M., Blinov, A., Kreikemeier, S.M., Chaplin, V., Keesan, M., Monroe, C., Kim, J.: Benchmarking an 11-qubit quantum computer. *Nature Communications* **10**, 5464 (2019) <https://doi.org/10.1038/s41467-019-13534-2>
- [4] Bruzewicz, C.D., Chiaverini, J., McConnell, R., Sage, J.M.: Trapped-ion quantum computing: Progress and challenges. *Applied Physics Reviews* **6**(2), 021314 (2019) <https://doi.org/10.1063/1.5088164>
- [5] Krantz, P., Kjaergaard, M., Yan, F., Orlando, T.P., Gustavsson, S., Oliver, W.D.: A quantum engineer’s guide to superconducting qubits. *Applied Physics Reviews* **6**(2), 021318 (2019) <https://doi.org/10.1063/1.5089550>

- [6] Browaeys, A., Lahaye, T.: Many-body physics with individually controlled Rydberg atoms. *Nature Physics* **16**(2), 132–142 (2020) <https://doi.org/10.1038/s41567-019-0733-z>
- [7] Evered, S.J., Bluvstein, D., Kalinowski, M., Ebadi, S., Manovitz, T., Zhou, H., Li, S.H., Geim, A.A., Wang, T.T., Maskara, N., Levine, H., Semeghini, G., Omran, A., Lukin, M.D.: High-fidelity parallel entangling gates on a neutral-atom quantum computer. *Nature* **622**(7982), 268–272 (2023) <https://doi.org/10.1038/s41586-023-06481-y>
- [8] D’Alessandro, D.: *Introduction to Quantum Control and Dynamics*. Chapman and Hall/CRC, Boca Raton (2007). <https://doi.org/10.1201/9781584888833>
- [9] Khaneja, N., Reiss, T., Kehlet, C., Schulte-Herbrüggen, T., Glaser, S.J.: Optimal control of coupled spin dynamics: design of NMR pulse sequences by gradient ascent algorithms. *Journal of Magnetic Resonance* **172**(2), 296–305 (2005) <https://doi.org/10.1016/j.jmr.2004.11.004>
- [10] Krotov, V.F.: *Global Methods in Optimal Control Theory*. Marcel Dekker, New York (1996)
- [11] Doria, P., Calarco, T., Montangero, S.: Optimal control technique for many-body quantum dynamics. *Physical Review Letters* **106**(19), 190501 (2011) <https://doi.org/10.1103/PhysRevLett.106.190501>
- [12] Niu, M.Y., Boixo, S., Smelyanskiy, V.N., Neven, H.: Universal quantum control through deep reinforcement learning. *npj Quantum Information* **5**, 33 (2019) <https://doi.org/10.1038/s41534-019-0141-3>
- [13] Porotti, R., Tamascelli, D., Restelli, M., Prati, E.: Coherent transport of quantum states by deep reinforcement learning. *Communications Physics* **2**, 61 (2019) <https://doi.org/10.1038/s42005-019-0169-x>
- [14] Bukov, M., Day, A.G.R., Sels, D., Weinberg, P., Polkovnikov, A., Mehta, P.: Reinforcement learning in different phases of quantum control. *Physical Review X* **8**(3), 031086 (2018) <https://doi.org/10.1103/PhysRevX.8.031086> [arXiv:1705.00565](https://arxiv.org/abs/1705.00565)
- [15] Metz, F., Bukov, M.: Self-correcting quantum many-body control using reinforcement learning with tensor networks. *Nature Machine Intelligence* **5**(7), 780–791 (2023) <https://doi.org/10.1038/s42256-023-00687-5> [arXiv:2201.11790](https://arxiv.org/abs/2201.11790)
- [16] Reuer, K., Landgraf, J., Fösel, T., O’Sullivan, J., Beltrán, L., Akin, A., Norris, G.J., Remm, A., Kerschbaum, M., Besse, J.-C., Marquardt, F., Wallraff, A., Eichler, C.: Realizing a deep reinforcement learning agent discovering real-time feedback control strategies for a quantum system. *Nature Communications* **14**, 7138 (2023) <https://doi.org/10.1038/s41467-023-42901-3> [arXiv:2210.16715](https://arxiv.org/abs/2210.16715)

- [17] Zen, R., Olle, J., Colmenarez, L., Puviani, M., Müller, M., Marquardt, F.: Quantum circuit discovery for fault-tolerant logical state preparation with reinforcement learning. *Physical Review X* **15**(4), 041012 (2025) [arXiv:2402.17761](https://arxiv.org/abs/2402.17761)
- [18] Judson, R.S., Rabitz, H.: Teaching lasers to control molecules. *Physical Review Letters* **68**(10), 1500–1503 (1992) <https://doi.org/10.1103/PhysRevLett.68.1500>
- [19] Leung, N., Abdelhafez, M., Koch, J., Schuster, D.: Speedup for quantum optimal control from automatic differentiation based on graphics processing units. *Physical Review A* **95**(4), 042318 (2017) <https://doi.org/10.1103/PhysRevA.95.042318>
- [20] Vaidhyanathan, P., Marquardt, F., Mitchison, M.T., Ares, N.: Quantum feedback control with a transformer neural network architecture. *Physical Review Research* **8**(1), 012043 (2026) <https://doi.org/10.1103/PhysRevResearch.8.L012043>
- [21] Schäfer, F., Kloc, M., Bruder, C., Lörch, N.: A differentiable programming method for quantum control. *Machine Learning: Science and Technology* **1**(3), 035009 (2020) <https://doi.org/10.1088/2632-2153/ab9802>
- [22] Coopmans, L., Luo, D., Kells, G., Clark, B.K., Carrasquilla, J.: Protocol discovery for the quantum control of majoranas by differentiable programming and natural evolution strategies. *PRX Quantum* **2**, 020332 (2021) <https://doi.org/10.1103/PRXQuantum.2.020332>
- [23] Porotti, R., Peano, V., Marquardt, F.: Gradient-ascent pulse engineering with feedback. *PRX Quantum* **4**(3), 030305 (2023) <https://doi.org/10.1103/PRXQuantum.4.030305> [arXiv:2203.04271](https://arxiv.org/abs/2203.04271)
- [24] Duncan, C.W., Poggi, P.M., Bukov, M., Zinner, N.T., Campbell, S.: Taming quantum systems: A tutorial for using shortcuts-to-adiabaticity, quantum optimal control, and reinforcement learning. *PRX Quantum* **6**(4), 040201 (2025) <https://doi.org/10.1103/PRXQuantum.6.040201>
- [25] Bukov, M., Marquardt, F.: Reinforcement Learning for Quantum Technology. Review article (2026)
- [26] Trinh, T.H., Wu, Y., Le, Q.V., He, H., Luong, T.: Solving olympiad geometry without human demonstrations. *Nature* **625**, 476–482 (2024) <https://doi.org/10.1038/s41586-023-06747-5>
- [27] Chen, M., Tworek, J., Jun, H., Yuan, Q., Pinto, H.P.d.O., Kaplan, J., et al.: Evaluating large language models trained on code. arXiv preprint [arXiv:2107.03374](https://arxiv.org/abs/2107.03374) (2021)
- [28] Romera-Paredes, B., Barekatin, M., Novikov, A., Balog, M., Kumar, M.P., Dupont, E., Ruiz, F.J.R., Ellenberg, J.S., Wang, P., Fawzi, O., Kohli, P., Fawzi, A.: Mathematical discoveries from program search with large language models.

- Nature **625**(7995), 468–475 (2024) <https://doi.org/10.1038/s41586-023-06924-6>
- [29] Yang, R., Wang, Z., Gu, Y., Chen, T., Liang, Y., Li, T.: QCircuitBench: A large-scale dataset for benchmarking quantum algorithm design. arXiv preprint arXiv:2410.07961 (2024). NeurIPS 2025
- [30] Arlt, S., Duan, H., Li, F., Xie, S.M., Wu, Y., Krenn, M.: Meta-designing quantum experiments with language models. Nature Machine Intelligence **8**, 148–157 (2026) [arXiv:2406.00626](https://doi.org/10.1038/s41586-023-06924-6)
- [31] Arlt, S., Gu, X., Krenn, M.: Towards autonomous quantum physics research using LLM agents with access to intelligent tools (2025)
- [32] Spall, J.C.: Multivariate stochastic approximation using a simultaneous perturbation gradient approximation. IEEE Transactions on Automatic Control **37**(3), 332–341 (1992) <https://doi.org/10.1109/9.119632>
- [33] Lu, P., Mishra, S., Xia, T., Qiu, L., Chang, K.-W., Zhu, S.-C., Tafjord, O., Clark, P., Kalyan, A.: Learn to explain: Multimodal reasoning via thought chains for science question answering. In: Advances in Neural Information Processing Systems (NeurIPS) (2022)
- [34] Hendrycks, D., Burns, C., Kadavath, S., Arora, A., Basart, S., Tang, E., Song, D., Steinhardt, J.: Measuring mathematical problem solving with the MATH dataset. NeurIPS (2021) [arXiv:2103.03874](https://arxiv.org/abs/2103.03874)
- [35] Li, A., Stein, S., Krishnamoorthy, S., Ang, J.: QASMBench: A low-level quantum benchmark suite for NISQ evaluation and simulation. ACM Transactions on Quantum Computing **4**(2) (2023) <https://doi.org/10.1145/3550488>
- [36] Quetschlich, N., Burgholzer, L., Wille, R.: MQT Bench: Benchmarking software and design automation tools for quantum computing. Quantum **7**, 1062 (2023) <https://doi.org/10.22331/q-2023-07-20-1062>
- [37] Perrier, E., Youssry, A., Ferrie, C.: QDataSet, quantum datasets for machine learning. Scientific Data **9**, 582 (2022) <https://doi.org/10.1038/s41597-022-01639-1>
- [38] Tang, Y., Xiong, H., Yang, N., Xiao, T., Yan, J.: Towards LLM4QPE: Unsupervised pretraining of quantum property estimation and a benchmark. In: International Conference on Learning Representations (ICLR) (2024)
- [39] Song, Z., Lu, J., Du, Y., Yu, B., Prunyn, T.M., Huang, Y., Guo, K., Luo, X., Qu, Y., Qu, Y., Wang, Y., Wang, H., Guo, J., Gan, J., Shojaei, P., Luo, D., Dillmann, S., Bran, A.M., Li, G., Zhao, Q., et al.: Evaluating Large Language Models in Scientific Discovery. Introduces the SDE (Scientific Discovery Evaluation) framework and the `sde-harness` project-level evaluation toolkit. (2025). <https://arxiv.org/abs/2512.15567>

- [40] BerriAI: LiteLLM: Open Source AI Gateway for 100+ LLM providers. <https://github.com/BerriAI/litellm>. Python SDK and proxy server providing a unified OpenAI-format interface to 100+ LLM providers. (2023)
- [41] Demirplak, M., Rice, S.A.: Adiabatic population transfer with control fields. *Journal of Physical Chemistry A* **107**(46), 9937–9945 (2003) <https://doi.org/10.1021/jp030708a>
- [42] Berry, M.V.: Transitionless quantum driving. *Journal of Physics A: Mathematical and Theoretical* **42**(36), 365303 (2009) <https://doi.org/10.1088/1751-8113/42/36/365303>
- [43] Dicke, R.H.: Coherence in spontaneous radiation processes. *Physical Review* **93**(1), 99–110 (1954) <https://doi.org/10.1103/PhysRev.93.99>
- [44] Landau, L.D.: Zur theorie der energieübertragung. II. *Physikalische Zeitschrift der Sowjetunion* **2**, 46–51 (1932)
- [45] Zener, C.: Non-adiabatic crossing of energy levels. *Proceedings of the Royal Society of London A* **137**(833), 696–702 (1932) <https://doi.org/10.1098/rspa.1932.0165>
- [46] Lindblad, G.: On the generators of quantum dynamical semigroups. *Communications in Mathematical Physics* **48**(2), 119–130 (1976) <https://doi.org/10.1007/BF01608499>
- [47] Gorini, V., Kossakowski, A., Sudarshan, E.C.G.: Completely positive dynamical semigroups of N-level systems. *Journal of Mathematical Physics* **17**(5), 821–825 (1976) <https://doi.org/10.1063/1.522979>
- [48] Coppersmith, D.: An approximate Fourier transform useful in quantum factoring. arXiv preprint arXiv:quant-ph/0201067 (2002). Originally IBM Research Report RC 19642 (1994)
- [49] Vitanov, N.V., Rangelov, A.A., Shore, B.W., Bergmann, K.: Stimulated Raman adiabatic passage in physics, chemistry, and beyond. *Reviews of Modern Physics* **89**(1), 015006 (2017) <https://doi.org/10.1103/RevModPhys.89.015006>
- [50] Weedbrook, C., Pirandola, S., García-Patrón, R., Cerf, N.J., Ralph, T.C., Shapiro, J.H., Lloyd, S.: Gaussian quantum information. *Reviews of Modern Physics* **84**(2), 621–669 (2012) <https://doi.org/10.1103/RevModPhys.84.621>
- [51] Toffoli, T.: Reversible computing. In: *Automata, Languages and Programming. Lecture Notes in Computer Science*, vol. 85, pp. 632–644. Springer, Berlin, Heidelberg (1980). https://doi.org/10.1007/3-540-10003-2_104
- [52] Koch, J., Yu, T.M., Gambetta, J., Houck, A.A., Schuster, D.I., Majer, J., Blais, A., Devoret, M.H., Girvin, S.M., Schoelkopf, R.J.: Charge-insensitive qubit design

- derived from the Cooper pair box. *Physical Review A* **76**(4), 042319 (2007) <https://doi.org/10.1103/PhysRevA.76.042319>
- [53] Motzoi, F., Gambetta, J.M., Rebentrost, P., Wilhelm, F.K.: Simple pulses for elimination of leakage in weakly nonlinear qubits. *Physical Review Letters* **103**(11), 110501 (2009) <https://doi.org/10.1103/PhysRevLett.103.110501>
- [54] Morris, G.A., Freeman, R.: Enhancement of nuclear magnetic resonance signals by polarization transfer. *Journal of the American Chemical Society* **101**(3), 760–762 (1979) <https://doi.org/10.1021/ja00497a058>
- [55] Carr, H.Y., Purcell, E.M.: Effects of diffusion on free precession in nuclear magnetic resonance experiments. *Physical Review* **94**(3), 630–638 (1954) <https://doi.org/10.1103/PhysRev.94.630>
- [56] Viola, L., Knill, E., Lloyd, S.: Dynamical decoupling of open quantum systems. *Physical Review Letters* **82**(12), 2417–2421 (1999) <https://doi.org/10.1103/PhysRevLett.82.2417>